

# Enhancing CAR Macrophage Efferocytosis Via Surface Engineered Lipid Nanoparticles Targeting LXR Signaling

Skylar T. Chuang, Joshua B. Stein, Sarah Nevins, Cemile Kilic Bektas, Hye Kyu Choi, Wan-Kyu Ko, Hyunjun Jang, Jihun Ha, and Ki-Bum Lee\*

The removal of dying cells, or efferocytosis, is an indispensable part of resolving inflammation. However, the inflammatory microenvironment of the atherosclerotic plaque frequently affects the biology of both apoptotic cells and resident phagocytes, rendering efferocytosis dysfunctional. To overcome this problem, a chimeric antigen receptor (CAR) macrophage that can target and engulf phagocytosis-resistant apoptotic cells expressing CD47 is developed. In both normal and inflammatory circumstances, CAR macrophages exhibit activity equivalent to antibody blockage. The surface of CAR macrophages is modified with reactive oxygen species (ROS)-responsive therapeutic nanoparticles targeting the liver X receptor pathway to improve their cell effector activities. The combination of CAR and nanoparticle engineering activated lipid efflux pumps enhances cell debris clearance and reduces inflammation. It is further suggested that the undifferentiated CAR-Ms can transmigrate within a micro-fabricated vessel system. It is also shown that our CAR macrophage can act as a chimeric switch receptor (CSR) to withstand the immunosuppressive inflammatory environment. The developed platform has the potential to contribute to the advancement of next-generation cardiovascular disease therapies and further studies include *in vivo* experiments.

implicates the role of impaired efferocytosis in the pathogenesis of atherosclerosis.<sup>[3]</sup> The upregulation of CD47, a “don’t eat me” signal, on lesion foam cells significantly impedes efferocytosis when these cells undergo apoptosis. ACs that are not readily cleared can undergo secondary necrosis and contribute to chronic inflammation by increasing cellular oxidative stress and releasing pro-inflammatory intracellular factors.<sup>[4]</sup> Moreover, cholesterol crystals (CC) that enrich lesion foam cells also contribute to inflammation through the NLRP3 inflammasome pathway.<sup>[5]</sup> Collectively, these inflammatory hallmarks (i.e., necrotic cell debris and CC) cascade to further lesion expansion, plaque destabilization, and thrombosis. Hence, efficient removal of these detrimental hallmarks can alleviate chronic inflammation and reduce the risks associated with cardiovascular disease (CVD). Although systemic administration of therapeutic agents such as CD47-blocking antibodies greatly improves efferocytosis and reduces plaque burden, it can lead to side effects such as

## 1. Introduction

Programmed cell removal (PrCR) mediated by macrophages is a dynamic physiological process that plays a key role in immunosurveillance and maintaining tissue homeostasis.<sup>[1]</sup> In particular, the clearance of apoptotic cells (ACs), or efferocytosis, is pivotal in the resolution phase of inflammation.<sup>[2]</sup> Recent evidence

implicates the role of impaired efferocytosis in the pathogenesis of atherosclerosis.<sup>[3]</sup> These side effects can be partially mitigated by targeted pro-efferocytic nanoparticles.<sup>[6]</sup> However, increased AC ingestion after CD47 blockade can lead to the accumulation of free cholesterol pools in the phagocyte and an increase in cholesterol burden, culminating in CC formation.<sup>[7]</sup> Thus, there is a clear need to improve the current understanding of the role of efferocytosis in atherosclerosis and further develop novel therapeutic strategies to improve this process.

Despite the success of cholesterol-lowering drugs such as statins and PCSK9 inhibitors in reducing the incidence of atherosclerosis, CVD remains the leading cause of death worldwide.<sup>[8]</sup> A promising new way to treat atherosclerosis is targeting the liver X receptor (LXR) pathway. LXR is a protein that regulates cholesterol metabolism and homeostasis. By activating LXR, we can increase the amount of cholesterol that is removed from lesion foam cells, which helps prevent the buildup of plaque in the arteries.<sup>[9]</sup> In addition to facilitating cholesterol efflux that alleviates excess free cholesterol burden, the LXR pathway is also linked to promoting a tolerogenic response in macrophages via efferocytosis. In particular, Mer tyrosine kinase (MerTK) plays a key role in mediating AC ingestion and suppression of inflammation in mice with lupus-like autoimmunity.<sup>[10]</sup>

S. T. Chuang, J. B. Stein, S. Nevins, C. Kilic Bektas, H. K. Choi, W.-K. Ko, H. Jang, J. Ha, K.-B. Lee  
 Department of Chemistry and Chemical Biology  
 Rutgers  
 The State University of New Jersey  
 123 Bevier Road, Piscataway, NJ 08854, USA  
 E-mail: [kblee@rutgers.edu](mailto:kblee@rutgers.edu)

 The ORCID identification number(s) for the author(s) of this article can be found under <https://doi.org/10.1002/adma.202308377>

© 2024 The Authors. Advanced Materials published by Wiley-VCH GmbH. This is an open access article under the terms of the [Creative Commons Attribution](https://creativecommons.org/licenses/by/4.0/) License, which permits use, distribution and reproduction in any medium, provided the original work is properly cited.

DOI: [10.1002/adma.202308377](https://doi.org/10.1002/adma.202308377)

Indeed, activation of LXR $\alpha$  is linked to a dampened inflammatory response and an anti-inflammatory M2 phenotype, which is believed to be atheroprotective.<sup>[11]</sup> However, clinical development of LXR agonists is hampered by off-target effects such as hepatic steatosis and hypertriglyceridemia.<sup>[12]</sup> Further, due to their inherent hydrophobic nature, CC are insoluble and difficult to remove using pharmacological means. Hydroxypropyl  $\beta$ -cyclodextrin (HP $\beta$ -CD) is shown to positively affect atherosclerosis regression by increasing free cholesterol conversion to oxysterols through the LXR pathway in macrophages and promoting reverse cholesterol transport (RCT) in vivo.<sup>[13]</sup> The hydrophobic cavity of HP $\beta$ -CD permits stable host–guest complex interaction between CD and cholesterol, consequently improving CC solubility and reducing CC-mediated damage and inflammation. However, systemic administration of CD can lead to toxicities, with ototoxicity being a major side effect.<sup>[14]</sup> To this end, various formulations of CD-based nanoparticles have been developed for targeted atherosclerosis therapy.<sup>[15]</sup> Although CD-based therapies can alleviate the burden of lipids in the body, macrophages with increased expression of CD47 have limited ability to target and engulf ACs with the assistance of CD47-based therapies.

Given the complex nature of atherosclerosis and the heavy involvement of the immune system, immunoengineering approaches that modulate or augment the functions of the immune cell effector of the lesion can offer more remarkable therapeutic outcomes. Engineered cell therapy, such as chimeric antigen receptor (CAR) T cell therapy, has reached critical success in the treatment of acute and relapsed lymphoblastic leukemia.<sup>[16]</sup> The programmable functions of CAR enable the selective elimination of target cells. The versatility of CAR engineering has recently been extended to non-oncology applications,<sup>[17]</sup> as well as other types of immune cells, such as NK cells and macrophages.<sup>[18]</sup> We speculated that CAR-engineered monocytes and macrophages (CAR-Ms) targeting ACs with elevated CD47 expression (CD47<sup>Hi</sup> ACs) could improve cell clearance and decrease inflammation. We chose macrophages as engineering targets due to i) the high affinity of circulating monocytes (prior to macrophage differentiation) to mobilize toward inflamed atherosclerotic regions, ii) the prominent role of macrophages as essential phagocytes in the lesion, and iii) the resilience of macrophages and their ability to produce anti-inflammatory cytokines upon ingestion of ACs.<sup>[19]</sup> CAR-Ms are also hindered by inflammatory signaling in the microenvironment. To overcome this limitation, our novel CAR-M also serves as a chimeric switch receptor (CSR) in which the usual CD47-SIRP $\alpha$  is a stimulatory rather than an inhibitory signal. We also engineer the CAR-M to serve as a drug carrier of cholesterol-dissolving small molecules. Nanoparticle backpacks do not interfere with ordinary cell function and have previously been demonstrated to increase the bioavailability of the encapsulated drug and enhance cellular effector functions.<sup>[20]</sup> Through selective receptor targeting, spatio-temporal control of drug release can be achieved.<sup>[21]</sup> For example, CAR T-cells backpacked with IL-15 super-agonist nanogels enhance T-cell expansion and overall therapeutic efficacy in vivo.<sup>[22]</sup> Hence, attaching nanoparticles made of HP $\beta$ -CD to CAR-Ms enables scientists and clinicians to make CAR-Ms more resistant to the accumulation of lipids over time after they ingest ACs.

To overcome the aforementioned obstacles in engineering immune cells for CVD treatment, we developed a novel nano-

immunoengineering platform composed of i) anti-CD47 CAR-Ms and ii) surface-anchored HP $\beta$ -CD lipid nanoparticles ( $\beta$ -CD LNPs) to target the hard-to-clear CD47<sup>Hi</sup> ACs (Figure 1a). We hypothesized that the clearance of CD47<sup>Hi</sup> ACs could be improved by dual anti-CD47 CAR and  $\beta$ -CD LNP engineering. The propensity of monocytes to localize to inflamed tissues allows them to serve as advanced cell-based-drug delivery vehicles in vivo. We reasoned that CAR-expressing monocytes could mediate phagocytosis against CD47<sup>Hi</sup> ACs upon differentiation into CAR macrophages in situ at the lesion site and serve as drug delivery vehicles. Lipid nanoparticles are the gold standard for targeted drug delivery.<sup>[23]</sup> One lipid nanoparticle in particular, the  $\beta$ -CD LNP, is composed of HP $\beta$ -CD modified with a ROS-sensitive moiety to hydrophobically pack inside the nanoparticle core.<sup>[24]</sup> HP $\beta$ -CD, released by the  $\beta$ -CD LNP under oxidative stress, solubilizes the CCs and increases oxysterol metabolism. Free HP $\beta$ -CD upregulates the LXR pathway in macrophages, which can promote apoptotic cell debris clearance<sup>[25]</sup> (Figure 1b). To achieve this goal, we combine genetic engineering and nanotechnology. We first design a chimeric antigen receptor corresponding to anti-CD47 to engulf ACs at the injury site. Next, we introduce the  $\beta$ -CD LNP as a nano-sized carrier to enhance the breakdown of lipids by activating LXR signaling, which helps in the engulfment of AC and CC. This “living factory” would ensure that macrophages can efficiently break down lipids without being dilapidated by the immune system. Such metabolic reprogramming will, in turn, lead to increased cholesterol efflux and limit the overall lipid burden without hindering CAR activity. In short, our nanoparticle-backpacking approach will reduce and protect against ongoing lipid burden to facilitate efferocytosis of CD47<sup>Hi</sup> ACs by our anti-CD47 CAR-M cells.

## 2. Results and Discussion

### 2.1. Synthesis and Characterization of $\beta$ -CD Lipid Nanoparticles ( $\beta$ -CD LNPs)

To synthesize  $\beta$ -CD LNPs for degrading CC, we adapted a previously reported synthesis of core–shell LNPs containing phenylboronic acid pinacol ester (PBAP)-modified  $\beta$ -CD cores (Figure S1a, Supporting Information).<sup>[26]</sup> The <sup>1</sup>H-NMR and FT-IR spectral data confirmed the chemical composition via signature peaks (Figure S1b,c, Supporting Information). PBAP-modified  $\beta$ -CD LNPs were prepared by nanoprecipitation (Figure S2a, Supporting Information), resulting in an average diameter of 150 nm, as visualized by transmission electron microscopy (TEM) (Figure S2b, Supporting Information). We also characterized the synthesized PBAP by chemical mapping via X-ray photoelectron spectroscopy (Figure S2c, Supporting Information), which supports the successful incorporation of PBAP-modified  $\beta$ -CD into the LNPs. The  $\beta$ -CD LNPs had low cytotoxicity in both THP-1 macrophages and human umbilical vein endothelial cells (HUVECs) (Figure S2d, Supporting Information), highlighting their biocompatibility in a vascular system. While the  $\beta$ -CD LNPs were highly stable under normal conditions, they readily degraded under different H<sub>2</sub>O<sub>2</sub> concentrations and released HP $\beta$ -CD (Figure S3a, Supporting Information). The PBAP-mediated reaction products were observed to be effective at scavenging reactive oxygen species (ROS), as was demonstrated in the rhodamine

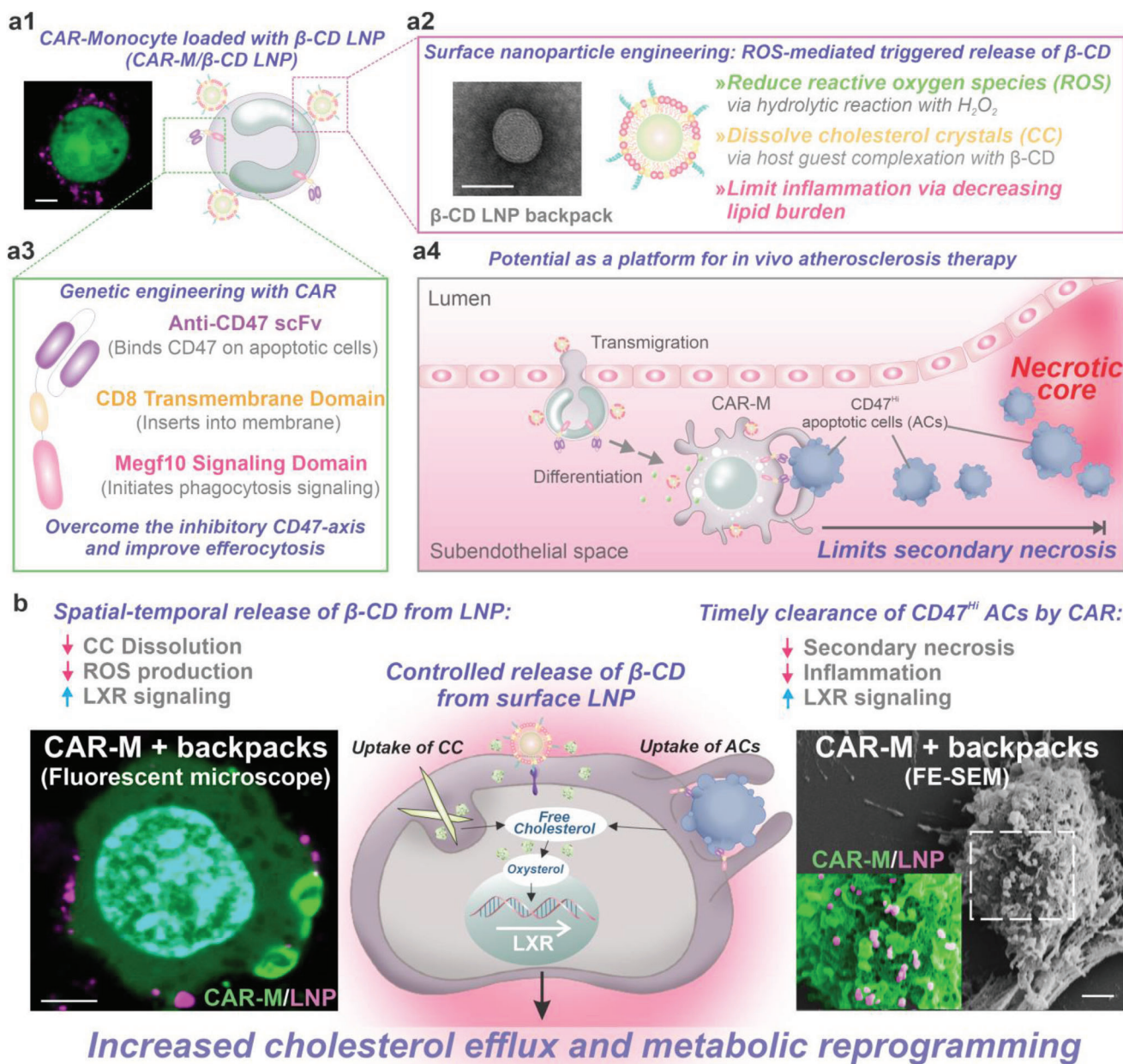


**Figure 1.** Nano-immunoengineered CAR-M for potential atherosclerosis therapy. a1) Schematic illustration of CAR-transduced THP-1 monocytes anchored with  $\beta$ -CD LNPs. The inset shows a confocal micrograph of CAR-monocyte carrying  $\beta$ -CD LNP backpacks. Scale bar is 5  $\mu$ m. a2) Schematic depiction and transmission electron micrograph of a  $\beta$ -CD LNP. Scale bar is 100 nm. a3) Design of the anti-CD47 CAR construct, a4) the  $\beta$ -CD LNP loaded CAR-Ms (CAR-M/ $\beta$ -CD LNP) could locate the inflamed lesion, traverse, and mediate targeted clearance of lesion apoptotic cells with elevated CD47 expression (CD47<sup>hi</sup> ACs). b) The ingested cholesterol-rich materials (ACs and CC) could be scavenged by  $\beta$ -CD released from cell surface LNPs due to ROS-mediated degradation. Oxysterols converted from cholesterol facilitated by  $\beta$ -CD could activate the LXR signaling pathway and increase key downstream genes such as *Abca1*, *Abcg1*, and *Mertk* to promote cholesterol efflux and suppression of inflammation. Scale bars are 5  $\mu$ m.

quenching assay (Figure S3b, Supporting Information) and reducing intracellular ROS (Figure S3c, Supporting Information). The ROS-scavenging effect of this material had been shown to reduce inflammation significantly and improve the therapeutic outcome in atherosclerosis and ischemic stroke.<sup>[15,27]</sup> Upon hydrolysis of the  $\beta$ -CD LNPs, the released HP $\beta$ -CD could readily form an

inclusion complex with cholesterol and effectively dissolve CC in a dose-dependent manner (Figure S4a, Supporting Information). Further, the  $\beta$ -CD LNP-treated macrophages harbored a lower amount of accumulated CC compared to the PBS-treated control macrophages (Figure S4b,c, Supporting Information). As the ability of the  $\beta$ -CD LNPs to partake in the LXR pathway was not

investigated previously,<sup>[15,27]</sup> we sought to evaluate this property using quantitative reverse transcription PCR (RT-qPCR). Treatment of CC-incubated THP-1 macrophages with  $\beta$ -CD LNPs led to a significant downregulation of the pro-inflammatory genes Il-1b, Nlrp3, and Il-6 by 2.95-, 3.27-, and 4.11-fold, respectively. Further, there was an upregulation of genes involved in cholesterol efflux (Abca1 and Abcg1, part of the LXR pathway) by 1.95- and 2.48-fold (Figure S4d, Supporting Information). A slight upregulation of Abca1 and Abcg1 by CC was also previously reported, and  $\beta$ -CD could further enhance such upregulation.<sup>[13]</sup>

## 2.2. In Vitro Anchoring of $\beta$ -CD LNPs onto THP-1 Monocytes and their Protective Effects

To allow controlled release of  $\beta$ -CD from the surface of monocytes, we chose CD45 as the target receptor for  $\beta$ -CD LNP binding because this receptor has been shown to permit surface retention of liposomes and nanogels for at least 7 days in T cells.<sup>[22]</sup> We first coupled anti-CD45 antibodies to the  $\beta$ -CD LNPs by thiol-maleimide coupling, followed by direct incubation with THP-1 monocytes to obtain  $\beta$ -CD LNP-bound cells<sup>[28]</sup> (Figure 2a).  $\beta$ -CD LNP backpacking on the CAR-M cell surface enabled the triggered release of HP $\beta$ -CD by the produced H<sub>2</sub>O<sub>2</sub> (intracellular or extracellular) in an inflammatory environment. DLS provided evidence of conjugation of the anti-CD45 antibodies by the increase in the hydrodynamic diameter of the  $\beta$ -CD LNPs after purification (Figure 2b). It is important to note that the  $\beta$ -CD LNPs were prepared with a negative zeta potential to prevent any nonspecific adsorption and subsequent endocytosis, which could reduce the amount of LNPs that could be retained at the surface. This method allowed for the loading of  $\beta$ -CD LNPs at different concentrations with various efficiencies (Figure 2c). Confocal microscopy revealed a robust loading of THP-1 monocytes with boron-dipyromethene-(BODIPY-) labeled  $\beta$ -CD LNPs (Figure 2d). The density of the  $\beta$ -CD LNPs could be tuned for optimal loading (Figure 2e). Based on the non-toxic concentration of 38  $\mu$ M (Figure S2d, Supporting Information), we chose this loading concentration for our subsequent experiments. Combined with the results of nanoparticle tracking analysis (NTA) (typical batch generates  $\approx 1.93 \times 10^9$  particles per mL), this was equivalent to  $\approx 174$  LNPs per cell. Previous studies have shown that up to 300 multilamellar liposomes could be tethered onto the surface of T cells.<sup>[20a]</sup> However, this could be due to a greater expression of CD45 on lymphocytes than on monocytes.<sup>[29]</sup> We further examined the targetability of CD45 as it was previously shown for NP retention in T cells. While there was no significant difference between the control group that contained no anti-CD45 antibody versus the group that contained the anti-CD45 antibody immediately after cell backpacking, we observed a drastic difference in the amount of cell-tethered NP fluorescence after 2 days post-anchoring (Figure 2f). Further, Z-stack imaging indicated the surface retention of the  $\beta$ -CD LNPs 2 days post-loading (Figure 2g). This highlights the pivotal role of targeted binding via CD45 conjugation in increasing the surface half-life of the  $\beta$ -CD LNPs in leukocytes. To further quantify the cell populations with surface  $\beta$ -CD LNPs over time, we employed flow cytometry to detect surface LNPs via biotin-streptavidin binding (Figure 2h). This enabled us to track

the number of surfaces versus internalized NP by examining the AlexaFluor to BODIPY fluorescence ratio. Most cells (>90%) exhibited NP on the surface after 1 day; however, there was a substantial decrease in the surface NP signature 2 days post-anchoring, according to Figure 2i. However, this is possibly attributed to the proliferative property of THP-1 cells in the undifferentiated state (proliferation time  $\approx 26$  h) that leads to the dilution of surface-bound  $\beta$ -CD LNPs. A similar finding is seen in primary T cells containing NP backpacks after stimulation in vitro.<sup>[20a]</sup>

Next, we sought to evaluate whether the release of HP $\beta$ -CD from  $\beta$ -CD LNP-backpacked cells could provide sufficient concentrations in reducing CC. We pre-loaded THP-1 cells with the LNPs and harvested cell supernatant at least 24 h post-loading before incubating with CC under various conditions (Figure 3a). The HP $\beta$ -CD released from the NP-bound cells could solubilize CC in vitro, especially in those that contained H<sub>2</sub>O<sub>2</sub>. We further examined whether cellular backpacking could provide any protective effects by challenging the cells with various inflammatory mediators (Figure 3b). The decrease in intracellular CC in backpacked cells versus non-backpacked cells mirrored the results in our in vitro CC dissolution experiment (Figure 3c). When examining the CC-induced inflammation response, we observed a decrease in gene expression of both Nlrp3 and Il-1b in THP-1 macrophages containing  $\beta$ -CD LNP backpacks compared to those without, supporting the protective effect of backpacking in decreasing the inflammasome response (Figure 3d). Considering that M1 macrophages are the most common subtype detected in atherosclerotic lesions and cause plaque destabilization,<sup>[30]</sup> we subjected to control and NP-bound THP-1 macrophages to LPS and IFN- $\gamma$  for 24 h after their initial differentiation for 2 days. We found that control M1 macrophages had more 2'-7'-Dichlorodihydrofluorescein diacetate (DCFDA) fluorescence signal than NP-backpacked M1 macrophages, which suggests that the NP-backpacking decreased intracellular ROS levels (Figure 3e). Similarly, we saw a reduction in lipid accumulation in oxidized low-density lipoprotein (ox-LDL)-treated control macrophages compared to the backpacked macrophages (Figure 3f). Significantly, this further manifested the ROS and lipid scavenging advantages of surface-engineered nanoparticle backpacks. During efferocytosis, free cholesterol from ACs contributed to the intracellular cholesterol pool, which could be toxic and lead to CC buildup. Given the multiple protective effects of  $\beta$ -CD LNPs, we speculated that the  $\beta$ -CD LNPs could enhance efferocytosis by virtue of promoting free cholesterol conversion to oxysterols such as 25- or 27-hydroxycholesterol and activating the LXR pathway.<sup>[13]</sup>

Hence, we examined whether the  $\beta$ -CD LNPs could enhance LXR signaling during efferocytosis. Upon incubation with ACs, we observed a 1.81- and 5.22-fold up-regulation of essential LXR target genes Abca1 and Abcg1; Cyp27a1, whose 27-hydroxycholesterol product is an endogenous ligand for LXR, was also increased by 1.71-fold (Figure 3g). Previous reports have shown that HP $\beta$ -CD could facilitate cholesterol egress from lysosomes through the upregulation of LAMP-1 and that  $\gamma$ -CD could promote lysosomal-ER association through cellular conduits.<sup>[31]</sup> Mechanistically, the ER-associated enzyme cholesterol 25-hydroxylase had been shown to promote efferocytosis and resolution of inflammation in mice with lung

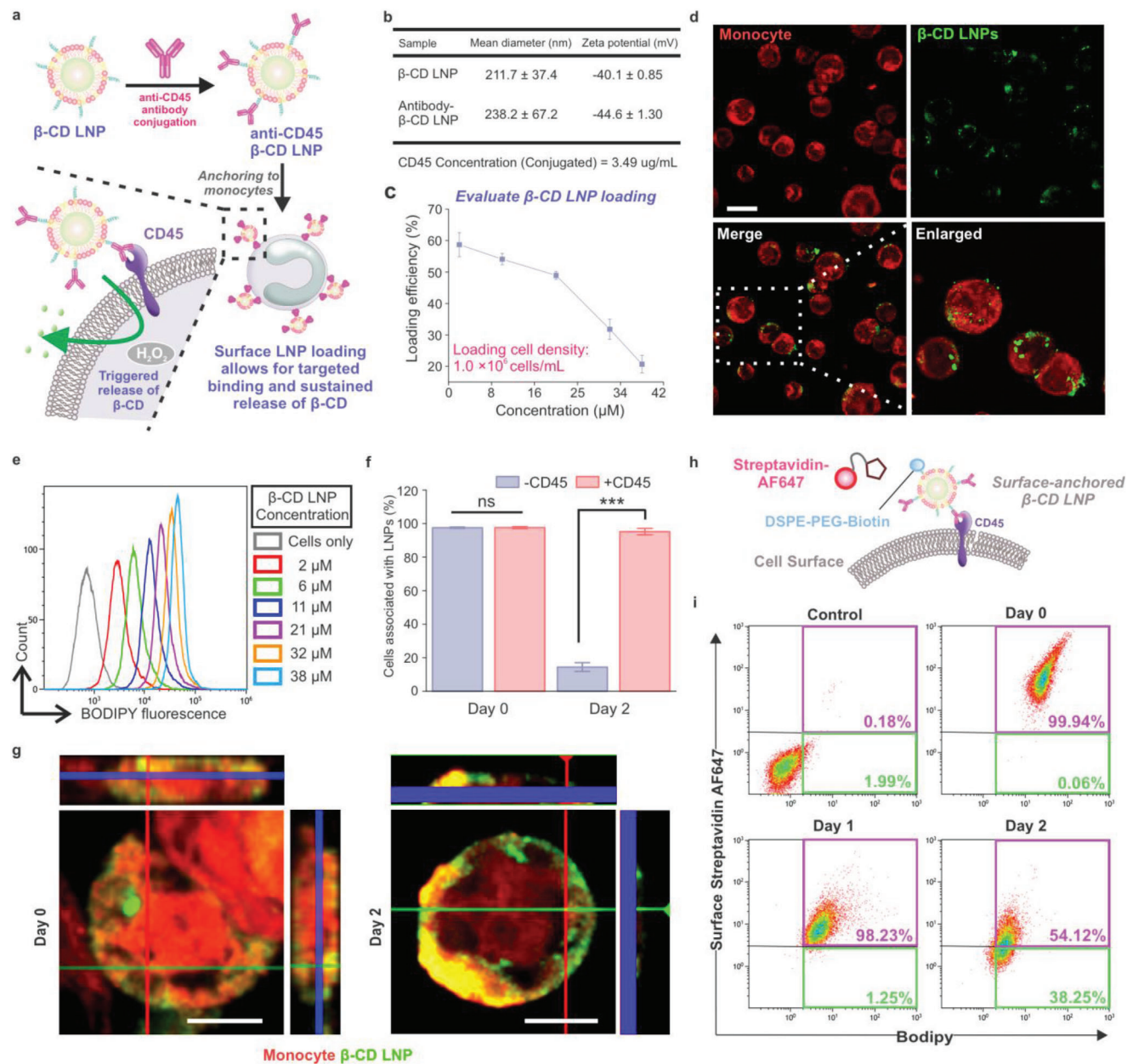


**Figure 2.** In-vitro surface anchoring of  $\beta$ -CD LNP onto monocytes. a) Schematic illustration of  $\beta$ -CD LNP loading onto THP-1 cells via CD45 targeting. b) Size and zeta potential change before and after CD45 antibody conjugation and antibody quantification. c) Loading efficiency of the  $\beta$ -CD LNPs based on a density of  $1.0 \times 10^6$  cells  $\text{mL}^{-1}$ . d) Confocal microscopy images of THP-1 cells (red) with  $\beta$ -CD LNP backpacks (green). Scale bar equals 20  $\mu\text{m}$ . e) THP-1 monocytes could be loaded with the indicated doses of  $\beta$ -CD LNPs and analyzed by flow cytometry. f, g) The effect of CD45 antibody targeting on cell-associated LNPs was evaluated on days 0 and 2 by flow cytometry (f) and confocal microscopy (g). Data represent mean  $\pm$  SEM;  $n = 3$ ; \*\*\* $p < 0.001$  by unpaired two-tailed Student's  $t$  test. Scale bars equal 5  $\mu\text{m}$ . h) Surface  $\beta$ -CD LNPs containing DSPE-PEG-biotin could be detected using a secondary reporter (AlexaFluor 647-streptavidin) by flow cytometry. i) Representative dot-plot of surface  $\beta$ -CD LNP on THP-1 cells over 2 days analyzed by flow cytometry.

inflammation;<sup>[32]</sup> while, the failure of lysosomal acid lipase-mediated production of 25- and 27-hydroxycholesterol was shown to reduce cholesterol efflux and efferocytosis.<sup>[33]</sup> In addition, there was a concomitant increase in Mertk and Il-10 by 1.57-fold and 2.85-fold in  $\beta$ -CD LNP-containing macrophages compared with unmodified macrophages (macrophages without backpacks), supporting enhanced efferocytosis. Notably, there

was also a reduction in Ccl2 expression, as well as an increase in the expression of Tfeb (autophagy marker) and Cd206 (M2 marker) expression. Collectively, these data demonstrate that  $\beta$ -CD LNP backpacks could reduce intracellular CC and the associated inflammation, offer protection against ROS and resistance to foam cell formation, and enhance efferocytosis while suppressing inflammation in THP-1 macrophages.

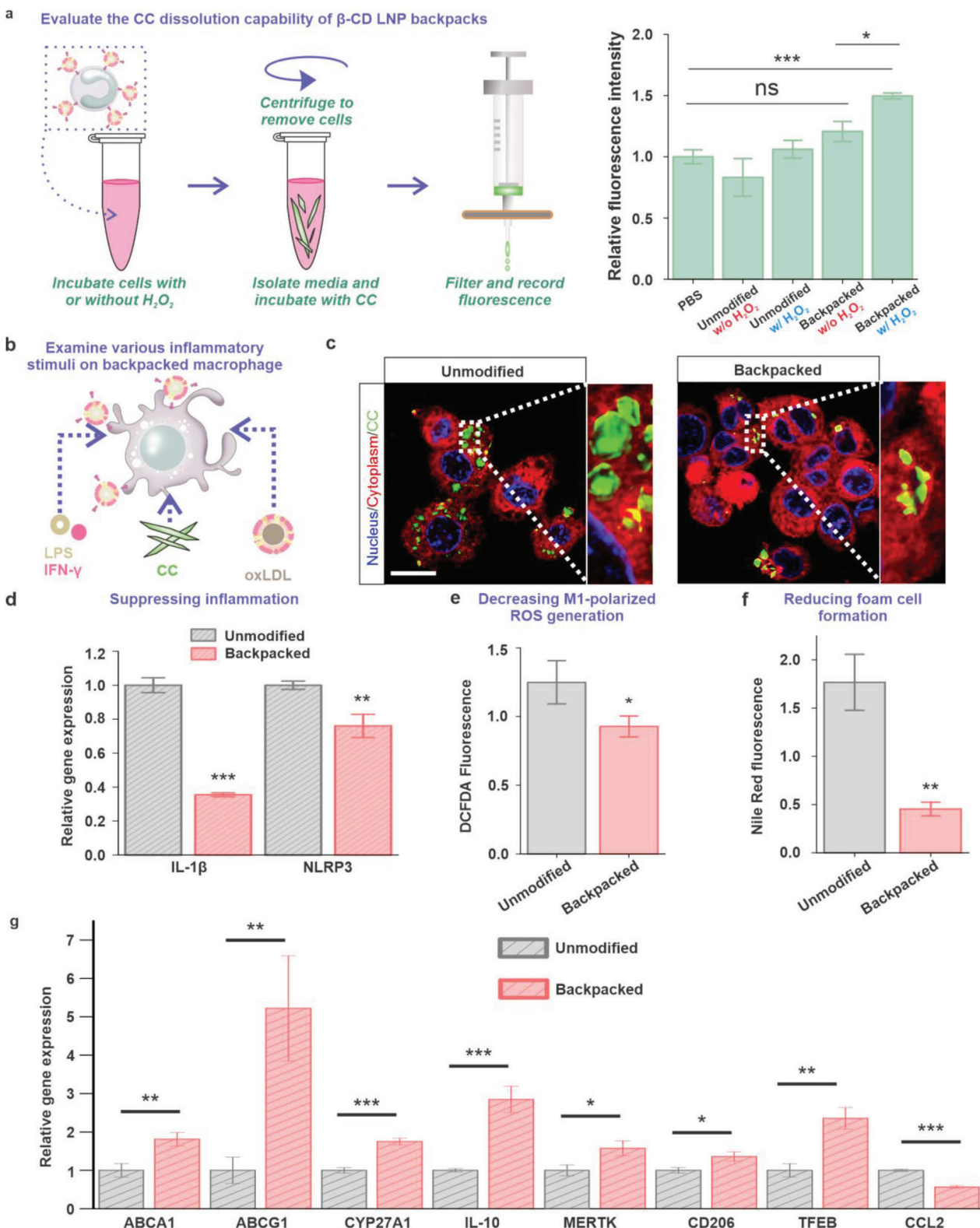


**Figure 3.**  $\beta$ -CD LNP loading mediates protection and potentiates efferocytosis in macrophages. a) Schematic depicting in vitro CC dissolution of THP-1 cells containing  $\beta$ -CD LNP backpacks. Data are mean  $\pm$  SEM;  $n = 3$ ; \* $p < 0.05$  and \*\*\* $p < 0.001$  by one-way ANOVA with Tukey post-hoc analysis; n.s. means no significance. b) THP-1 cells with or without  $\beta$ -CD LNP backpacks were challenged with various inflammatory mediators (LPS and IFN- $\gamma$ ; CC; oxLDL) to evaluate the protective effects of  $\beta$ -CD. c) Confocal microscopy images of THP-1 macrophages (red) examined 16 h after incubation with CC (green). Scale bar = 20  $\mu$ m. d) Canonical inflammasome genes in THP-1 macrophages after 3 h incubation with CC determined by RT-qPCR. e) DCFDA

### 2.3. CAR-M Engineering and Phagocytosis of CD47<sup>Hi</sup> AC Under Normal and Inflammatory Conditions

The main goal of this experimental design was to increase the LXR signaling further and the efferocytosis connection found through  $\beta$ -CD LNPs by manipulating the cells. A key underlying mechanism leading to defective efferocytosis in atherosclerosis is the upregulation of CD47, a myeloid immune checkpoint, in lesion smooth muscle cells.<sup>[3]</sup> Previous works have demonstrated the pivotal role TNF- $\alpha$  plays in upregulating CD47 expression in various types of cells via the NF- $\kappa$ B signaling pathway.<sup>[34]</sup> This event negatively impacts phagocytosis and AC clearance, leading to secondary necrosis in the atherosclerotic plaque. We hypothesized that by engineering macrophages with anti-CD47 CAR, we could enhance the phagocytosis of CD47<sup>Hi</sup> ACs. To increase macrophage efferocytic ability against CD47<sup>Hi</sup> ACs, we engineered human THP-1 monocytes with a first-generation, bicistronic lentiviral vector encoding a humanized anti-CD47 single chain antibody variable fragment (scFv), CD8 transmembrane domain, and a CD3 $\zeta$  intracellular domain linked to an EGFP reporter (Figure 4a,b). The CD3 $\zeta$  domain was previously shown to trigger phagocytosis due to the presence of immunoreceptor tyrosine-based activation motifs (ITAMs).<sup>[18c]</sup> Upon lentiviral transduction and FACS, the expression of CAR was evaluated using Protein L, which recognized immunoglobulin light chains and scFvs.<sup>[35]</sup> We chose Protein L rather than CD47 for CAR detection because the cognate receptor of CD47, SIRP $\alpha$ , was also expressed in macrophages; and thus, could interfere with evaluation. Flow cytometry analysis revealed that most of the population (83.7%) were double positive for GFP and Protein L-Alexa Fluor 647 after FACS (Figure 4c). There was also a small population of cells (7.7%) that were GFP-positive but not stained by Protein-L, possibly due to the very low surface expression of CAR. In contrast, the unsorted batch only contained 6.8% of double-positive cells. Thus, with the dual detection of the surrogate marker (GFP) and Protein L, we could confirm the surface expression of CAR in CAR-Ms.

One unique aspect of our CAR design is that it permits rewiring the endogenous inhibitory response upon CD47 binding. We speculated that the CAR-Ms could engulf the target CD47<sup>Hi</sup> ACs upon binding to CD47, which normally transduced an inhibitory signal to the host phagocyte. This concept of chimeric switch receptor (CSR) has previously been demonstrated in CAR T-cells against PD-L1,<sup>[36]</sup> but not in macrophages (Figure 4d). To test our hypothesis, we first prepared beads coated with lipids and CD47 proteins to mimic apoptotic bodies; then, we performed bead phagocytosis assays with the CAR-Ms (Figure S5a, Supporting Information). In contrast to the control macrophages transduced with a blank virus, the CAR-Ms took up a significantly greater number of CD47-coated beads (Figure S5b,c, Supporting Information). To further evaluate the phagocytic capability of CAR-Ms, we chose MCF-7 cells as model target ACs due to their high basal expression of CD47. Their surface ex-

pression of CD47 could be further increased by incubation with TNF- $\alpha$  before subjecting the cells to apoptosis for 4 h.<sup>[34]</sup> This allowed us to generate phagocytosis-resistant, CD47<sup>Hi</sup> early ACs that mimicked those found in chronically inflamed lesions.<sup>[3]</sup> We independently verified the upregulation of CD47 in MCF-7 cells by fluorescence microscopy under healthy and apoptotic conditions (Figure S6a, Supporting Information).

Further, flow cytometry showed a blunted reduction of CD47 on the surface of TNF- $\alpha$ -treated ACs (Figure S6b, Supporting Information). Interestingly, TNF- $\alpha$  treated cells not only showed increased fluorescence signal but also exhibited more clusters (Figure S6c, Supporting Information). The differential clustering of CD47 under healthy versus apoptotic states was described previously<sup>[37]</sup> and could also partially explain the increased resistance of ACs against clearance by macrophages under inflammatory conditions. Having established the target cell model, we first performed phagocytosis of CD47<sup>Hi</sup> ACs with control macrophages or CAR-Ms, using anti-CD47 antibodies as a positive control. After 1 h of incubation, there was very little phagocytosis in control macrophages (Figure 4e); in contrast, control macrophages with CD47-blocked ACs showed enhanced phagocytosis, with several whole cells in the process of being engulfed by the macrophages. When utilizing CAR-Ms, we noticed not only the occurrence of whole-cell engulfment but also the internalization of multiple cell “fragments” or apoptotic bodies. Confocal microscopy showed that the ACs were indeed internalized using Z-stack imaging (Figure S5d, Supporting Information). Next, we extended the phagocytosis experiment duration to 2 h because a typical phagocytosis event is usually completed within 30–180 min.<sup>[38]</sup> Compared to the control macrophages, there was a much greater phagocytosis of the CD47<sup>Hi</sup> ACs by CAR-Ms (Figure 4f). To further examine the phagocytosis events, we quantified the events using CellTagging, an image-based method previously reported by the Morris group.<sup>[39]</sup> This enabled us to distinguish the amount of CD47<sup>Hi</sup> ACs that were either partially engulfed or fully engulfed by the macrophages (Figure S7, Supporting Information). After 2 h of co-culture, we observed 69.8%  $\pm$  17.8% of CAR-Ms having engulfed one or more ACs, with 39.8%  $\pm$  3.41% of cells undergoing engulfment; on the other hand, only 34.9%  $\pm$  9.48% of control macrophages showed engulfment, in which 13.1%  $\pm$  6.07% of control cells had totally engulfed the target and 21.8%  $\pm$  4.00% of cells in the process of engulfing the ACs (Figure 4g–i)

The chronic inflammatory environment negatively affects both the capacity of the macrophages to carry out phagocytosis and the ability of the ACs to be cleared (Figure 5a). In addition to the overexpression of CD47 on ACs, lesion macrophages suffer reduced efferocytic capability due to ectodomain shedding of the tyrosine kinase receptors (i.e., TAM receptors, Tyro3, Axl, and MerTK) mediated by metalloproteinases such as A Disintegrin And Metalloprotease 17 (ADAM17), the expression of which can be upregulated with LPS.<sup>[40]</sup> Having demonstrated the potential

fluorescence of THP-1 macrophages as a measure of intracellular ROS levels after 24 h of stimulation with LPS (100 ng mL<sup>-1</sup>) and IFN- $\gamma$  (50 ng mL<sup>-1</sup>). f) Nile red fluorescence of THP-1 to assess lipid content in THP-1 macrophages. g) Gene expression changes in THP-1 macrophages with or without  $\beta$ -CD LNP backpacks incubated with apoptotic Jurkat cells (ACs) determined by RT-qPCR. Data represent mean  $\pm$  SEM;  $n = 3$ ; \* $p < 0.05$ , \*\* $p < 0.01$ , and \*\*\* $p < 0.001$  by unpaired two-tailed Student's  $t$ -test.

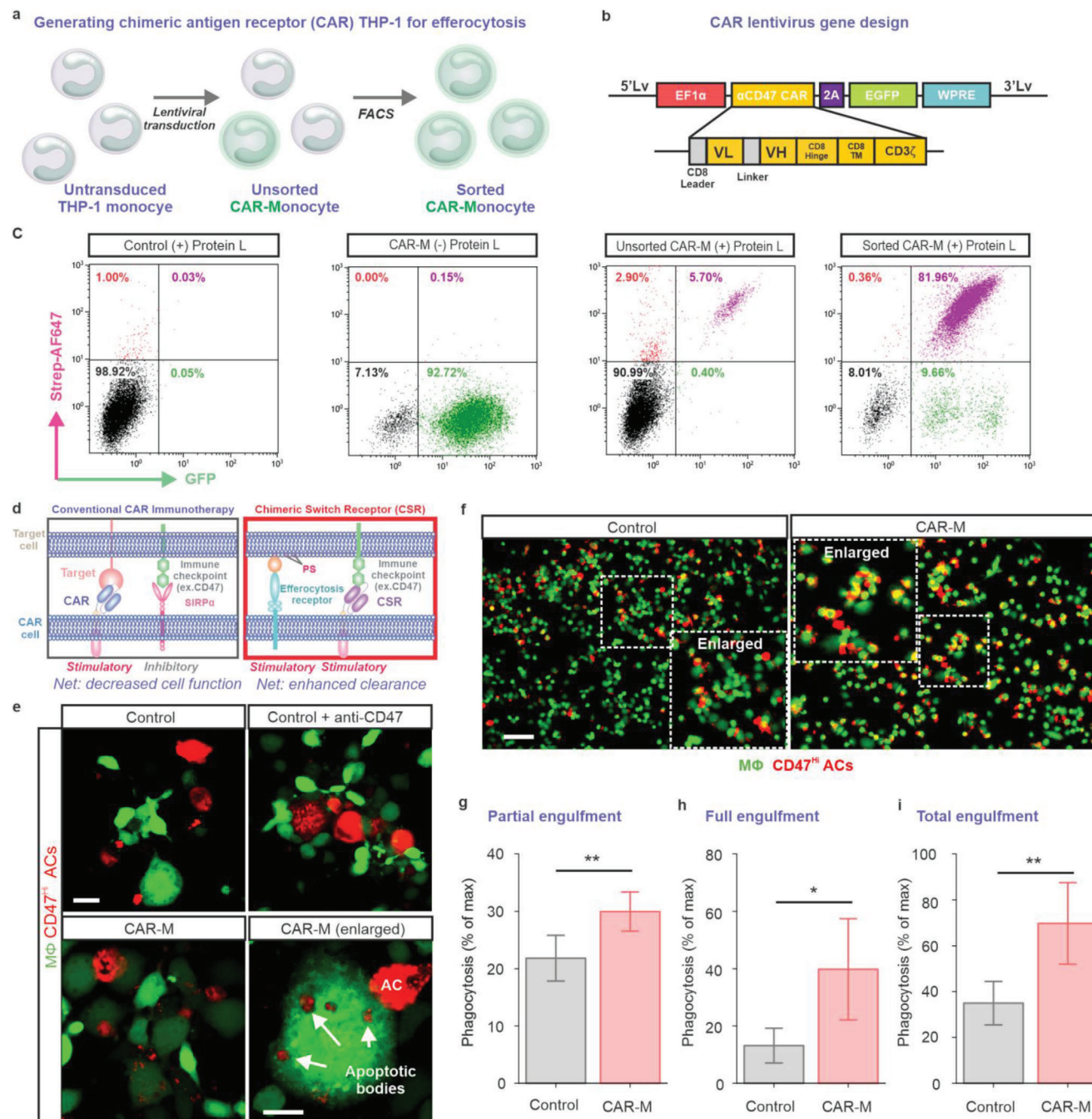


**Figure 4.** CAR-M engineering and phagocytosis activity. a) Schematic diagram illustrating the process of generating CAR-Ms from THP-1 cells. b) Lentiviral construct used for CAR transduction. c) Verification of surface expression of anti-CD47 CAR in CAR-Ms. d) The anti-CD47 CAR represents a chimeric switch receptor (CSR) that reverses existing inhibitory signal mediated by the SIRP $\alpha$ -CD47 axis to enhance phagocytosis of CD47<sup>Hi</sup> ACs. e) Confocal micrographs depicting phagocytosis of CD47<sup>Hi</sup> ACs in control macrophages, macrophages with CD47-blocked ACs, and CAR-Ms after 1 h incubation at 37 °C. Scale bar equals 20 μm. f) Representative fluorescence microscopy images of control macrophages and CAR-Ms incubated with ACs for 2 h at 37 °C. The cells were washed three times prior to imaging. Scale bar = 100 μm. g–i) Quantitative analysis of partial (g), full (h), and total (i) engulfment of CD47<sup>Hi</sup> AC using CellTagging after 2 h co-culture at 37 °C. Data are mean  $\pm$  SEM;  $n = 5$ ; \* $p < 0.05$  and \*\* $p < 0.01$  by unpaired two-tailed Student's  $t$ -test.

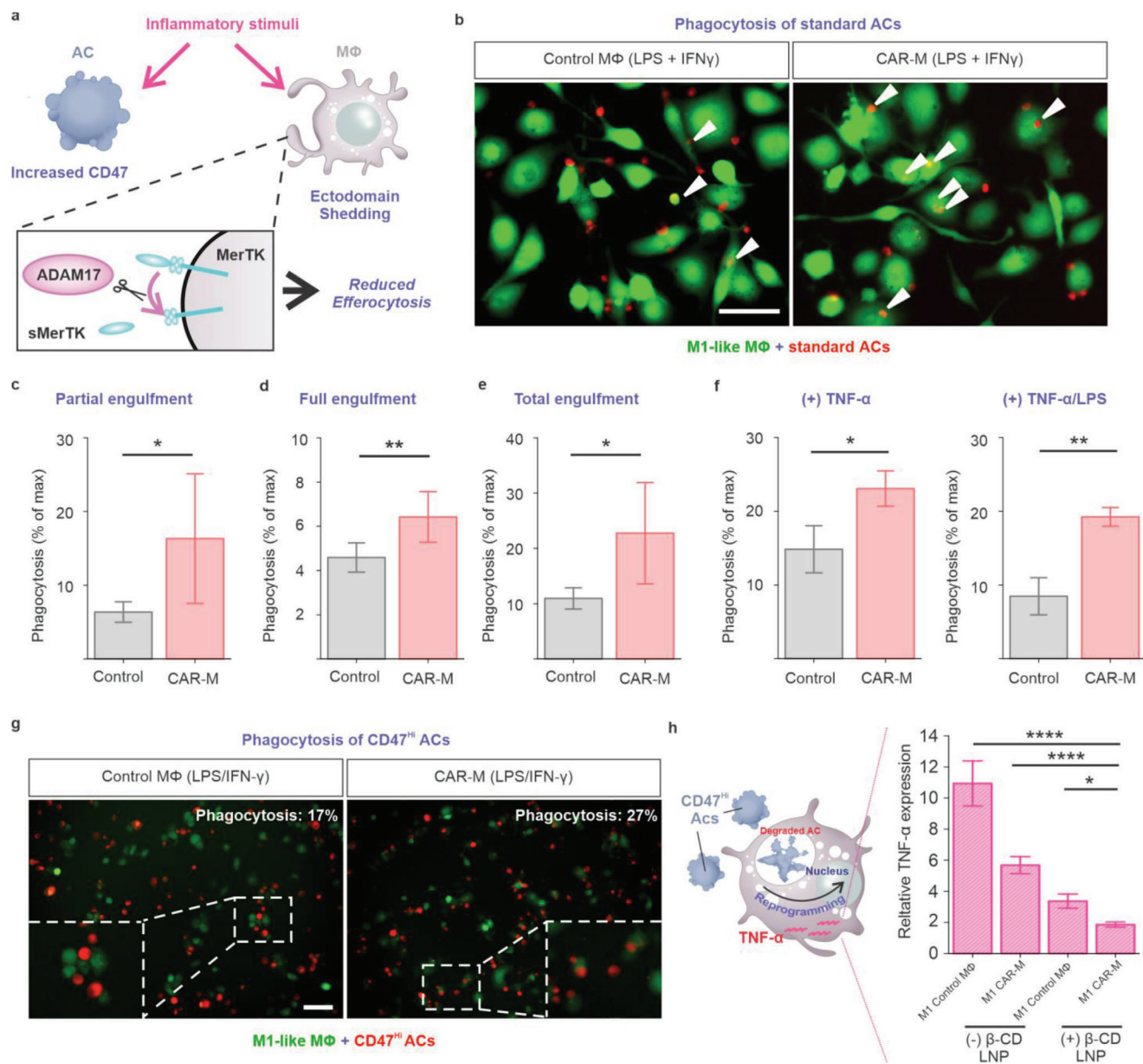


**Figure 5.** CAR-M phagocytosis under inflammatory condition. a) In addition to increasing CD47 expression in lesion cells, chronic inflammation also reduces the capacity of macrophages to clear ACs via ectodomain shedding. Efferocytic receptors (ex. MerTK) can be cleaved by metalloproteinase ADAM17, leading to reduced efferocytosis overall. b) Representative fluorescence micrographs depicting phagocytosis of standard ACs (without inducing CD47 elevation) by M1-control macrophages or CAR-Ms after 2 h incubation. Arrowheads point to fully internalized ACs. Scale bar = 100  $\mu$ m. c–e) Quantification of partial (c), full (d), and total internalization of standard ACs by either M1 control macrophages or CAR-Ms by CellTagging (e). f) Quantitative analysis of phagocytosis of standard ACs by control macrophages or CAR-Ms pretreated with either TNF- $\alpha$  alone or TNF- $\alpha$  and LPS. Data are mean  $\pm$  SEM;  $n = 3$ ; \* $p < 0.05$  and \*\* $p < 0.01$  by unpaired two-tailed Student's  $t$ -test. g) Combined M1 macrophages with CD47<sup>Hi</sup> ACs co-culture to simulate the phagocytosis in the atherosclerotic lesion environment. Scale bar = 100  $\mu$ m. h) Suppression of TNF- $\alpha$  expression in macrophages upon efferocytosis with CD47<sup>Hi</sup> ACs characterized by RT-qPCR. Data are mean  $\pm$  SEM;  $n = 3$ ; \* $p < 0.05$  and \*\* $p < 0.01$  by one-way ANOVA with Tukey post-hoc analysis.

of anti-CD47 CAR in enhancing the phagocytosis of CD47<sup>Hi</sup> ACs, we hypothesize that the anti-CD47 CAR can also serve as alternative receptors to rescue efferocytosis because of the loss in binding affinity between host SIRP $\alpha$  and CD47 on the surface of ACs.<sup>[37]</sup> To test this hypothesis, we subject both the control macrophages and CAR-M to various types of inflammatory sig-

nals without perturbing the levels of CD47 on ACs. We first simulate the inflammatory environment of the lesion by incubating phagocytes with LPS and IFN- $\gamma$  to induce M1 polarization. We subsequently prepared standard ACs from Jurkat cells (i.e., without inducing elevated CD47 expression) using established methods for co-culture experiments. We observe that while both M1

control macrophages and CAR-Ms exhibit reduced phagocytosis, CAR-Ms can phagocytose more Jurkat ACs (Figure 5b). Further analysis reveals  $6.42\% \pm 1.15\%$  and  $16.3\% \pm 8.81\%$  of M1 CAR-M partaking in full and partial engulfment, respectively, compared to  $4.59\% \pm 0.66\%$  and  $6.37\% \pm 1.39\%$  of M1 control macrophages engaged in such processes (Figure 5c–e). Similarly, while control macrophages and CAR-Ms exposed to either TNF- $\alpha$  alone or TNF- $\alpha$  and LPS exhibit reduced phagocytosis, CAR-Ms outperform control macrophages in phagocytosis ( $23.1\% \pm 2.40\%$  for TNF- $\alpha$  alone and  $19.2\% \pm 1.27\%$  for TNF- $\alpha$  and LPS in CAR-M;  $14.8\% \pm 3.19\%$  for TNF- $\alpha$  alone and  $8.47\% \pm 2.52\%$  for TNF- $\alpha$  and LPS in control macrophages (Figure 5f)).

To further examine the full extent of phagocytosis under inflammatory conditions, we sought to determine M1 CAR-M versus M1 control macrophage-mediated phagocytosis of CD47<sup>Hi</sup> ACs because CAR-Ms would be subjected to a similar inflammatory onslaught as endogenous lesion macrophages. Fluorescence microscopy showed  $\approx 27\%$  of M1 CAR-Ms having engulfed CD47<sup>Hi</sup> ACs, compared to  $\approx 17\%$  in control macrophages in 2 h (Figure 5g). Further, RT-qPCR analysis showed the most significant reduction of TNF- $\alpha$  in the M1 CAR-M/ $\beta$ -CD LNP group compared to other conditions (Figure 5h). This result also indirectly confirmed the timely phagocytosis of ACs because phagocytosis of necrotic cells leads to increased production of TNF- $\alpha$ .<sup>[37]</sup> Together, our data indicate that anti-CD47 CAR not only exerted improved phagocytosis of hard-to-clear CD47<sup>Hi</sup> ACs in CAR-M but could also serve as alternative receptors to induce target cell engulfment in different types of ACs.

## 2.4. Combining $\beta$ -CD LNPs With CAR-M for Enhanced Phagocytosis and Transmigration in a Microfabricated System

To better understand how CAR-Ms compare with the standard regimen of CD47 blockade, and whether  $\beta$ -CD LNPs could enhance the phagocytosis activity, we again investigated the degree of total, full, and partial phagocytosis of CD47<sup>Hi</sup> ACs (Figure 6a). Quantification analysis revealed increased phagocytosis in both control macrophages treated with anti-CD47 antibodies, CAR-Ms, and CAR-Ms/ $\beta$ -CD LNPs (Figure 6b–d). Although there was no statistically significant difference in total engulfment between the CAR-M versus CD47 blockade group ( $p = 0.29$ ), there was significantly greater phagocytosis in CAR-M/ $\beta$ -CD LNPs compared to control macrophages with anti-CD47 antibodies ( $p = 0.0071$ ), implying some synergy between CAR-mediated phagocytosis and the HP $\beta$ -CD released from LNPs. This enhancement mirrors the increase in anti-inflammatory cytokine expression after efferocytosis results from our in vitro  $\beta$ -CD LNP backpack experiments (Figure 4h). To confirm the enhancing effect of the engineered CAR, we performed RT-qPCR of control macrophages and CAR-Ms loaded with  $\beta$ -CD LNPs after phagocytosis of CD47<sup>Hi</sup> ACs. We observed an increased expression of the LXR target genes *Abca1* and *Abcg1* in CAR-Ms by 2.39- and 2.03-fold, respectively. Further, *Mertk* and *Il-10* levels increased by 1.42- and 2.21-fold compared to control macrophages with  $\beta$ -CD LNPs (Figure 6e). Live imaging further confirmed the timely reduction of ACs by CAR-M/ $\beta$ -CD LNP within 1 h (Figure 6f). Together, these findings provide evidence for a synergistic enhancement of efferocytosis by dual nanoparticle and CAR engi-

neering. One key advantage of a cell-based therapy platform is the homing ability of cells to target tissues. Monocytes have the ability to travel to atherosclerosis-affected areas by binding to activated endothelial cells and then passing through the endothelial layer into the subendothelial layer (diapedesis), as illustrated in Figure S8a, Supporting Information. To demonstrate the feasibility of CAR-Ms as a potential therapeutic platform in a vascular system, we first tested the cytotoxicity of CAR-Ms by performing co-culturing experiments with HUVECs. We opted for 50/50 culture media for the greatest viability of THP-1 and HUVECs. This resulted in an  $\approx 14\%$  reduction in the cell viability of HUVECs. Considering this, no observable toxicity was associated with HUVECs co-incubated with CAR-Ms after 24 h (Figure S8b, Supporting Information). Having confirmed the non-toxic nature of CAR-Ms, we next evaluated the conditions for optimal HUVEC activation for cell binding by treating the cells with TNF- $\alpha$  at different dosages for different time points (Figure S8c,d, Supporting Information). The subendothelial space or arterial intima was heavily comprised of extracellular matrix materials, such as collagen, fibronectin, and laminin. For the CAR-Ms to function as intended, we performed preliminary cell penetration and migration studies using gelatin–methacrylate (GelMA) hydrogels. Initial attempts using 10% cross-linked GelMA did not result in meaningful penetration or migration. Adjusting the cross-linked concentration to 6% and adding ACs resulted in more significant cell migration (Figure S8e, Supporting Information). With that, we constructed a microfluidic device to examine the adhesion and trans-endothelial migration of CAR-Ms (Figure 6g) (Figure S8f, Supporting Information). The device was constructed with one pathway to allow for the seeding and adhesion of HUVECs and a second channel that was filled with GelMA containing ACs, replicating the subendothelial space of atherosclerotic plaque tissue. Next, we developed an optimized procedure for cell seeding, hydrogel loading, and cell activation (Figure 6h). Upon 24 h of co-incubation, we could readily observe the binding of CAR-Ms with the activated HUVECs, as similarly shown in control THP-1 monocytes (Figure 6i). To demonstrate the potential of CAR-Ms in acting as therapeutic vehicles, we anchored  $\beta$ -CD LNP backpacks onto the cells and examined diapedesis. Confocal microscopy revealed an increased number of CAR-Ms transmigrated to the GelMA layer in the activated HUVEC group compared to the non-activated group, demonstrating the potential of the LNP-loaded CAR-Ms as a platform for targeting inflamed atherosclerotic lesions in vivo (Figure 6j). While our microfluidic device showed the ability of our CAR-M cells to migrate to the GelMA layer of the microfluidic device, more experiments are required to correlate these findings to the context of atherosclerotic plaque.

## 3. Conclusion

Given that macrophages play a profound role in the catabolic turnover of cellular materials in the peripheral tissues, our objective was to enhance the capabilities of macrophages to clear ACs that overexpress CD47 because of chronic inflammation. To achieve this, we developed a new type of CAR-Ms called the chimeric switch receptor macrophage (CSR-M). Our approach combined the anti-CD47 scFv with a stimulatory intracellular signaling domain, effectively reversing the inhibitory signaling

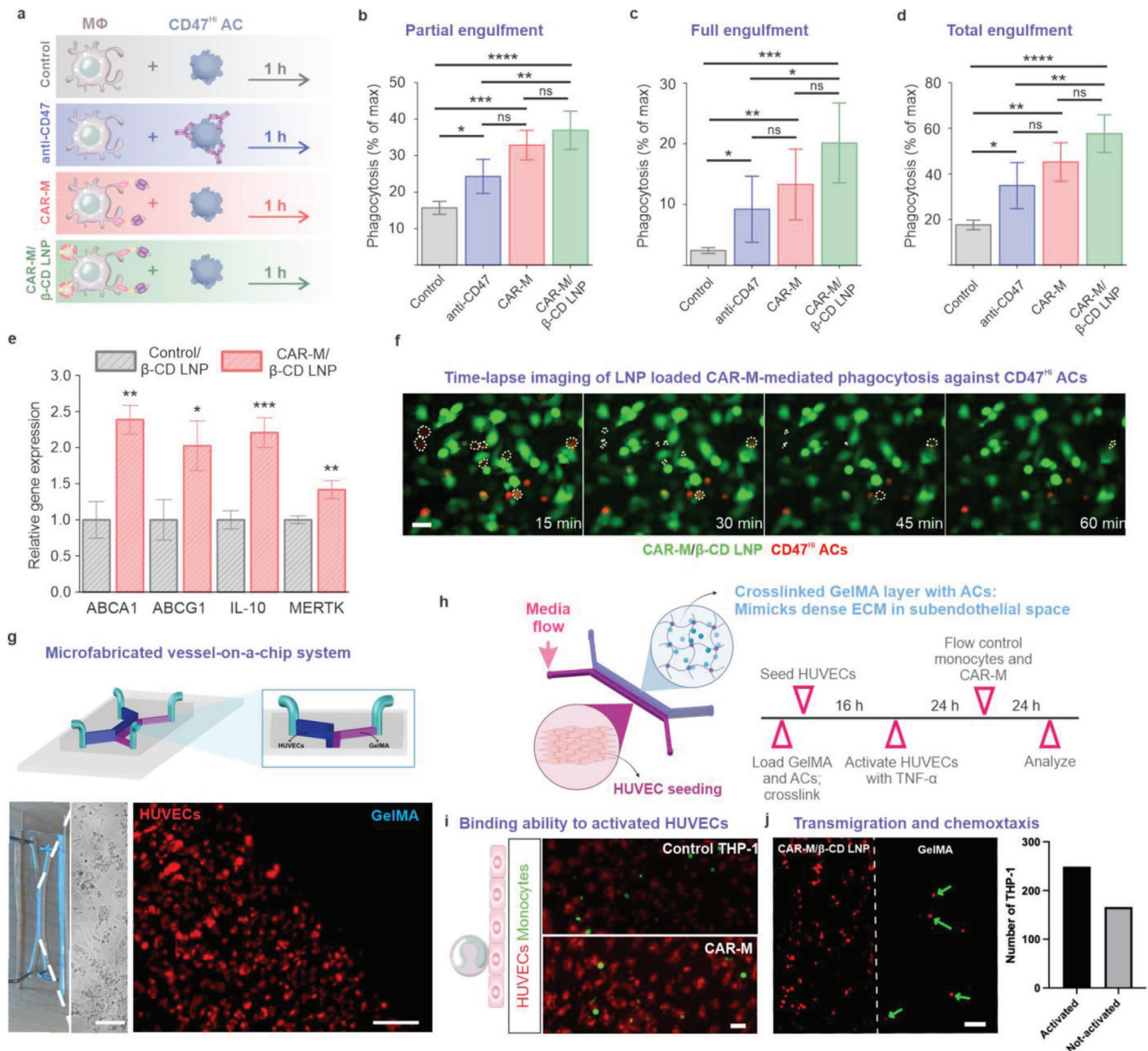


**Figure 6.** Assessment of CAR-M phagocytosis combined with  $\beta$ -CD LNP. a) The various conditions selected to evaluate macrophage phagocytosis of CD47<sup>Hi</sup> AC. Quantitative analysis via CellTagging of b) partial, c) full, and d) total engulfment after 1 h incubation of macrophage with CD47<sup>Hi</sup> AC at 37 °C. e) The activation of LXR signaling targets *Abca1* and *Abcg1* as well as efferocytosis targets *Il-10* and *Mertk* in control macrophages with  $\beta$ -CD LNPs or CAR-Ms with  $\beta$ -CD LNPs after co-culture with CD47<sup>Hi</sup> AC for 2 h at 37 °C. f) Time lapse fluorescence imaging of CAR-Ms with CD47<sup>Hi</sup> AC for 1 h. Scale bar equals 45  $\mu$ m. g) (top) 3D rendering of the microfabricated vessel-on-a-chip device constructed using photolithography; (bottom) HUVECs were seeded in the top channel and visualized by microscopy. Scale bars equal 100  $\mu$ m. h) Experimental timeline for HUVEC activation and CAR-M co-culture. i) Fluorescence microscopy images examining the adherence of control THP-1 cells and CAR-Ms to TNF- $\alpha$ -activated HUVECs in the device. Scale bars = 20  $\mu$ m. j) Confocal microscopy image and quantitation of CAR-Ms in the GelMA hydrogel layer indicating transendothelial migration. The CAR-Ms were fluorescently labeled with  $\beta$ -CD LNPs (red). Scale bar = 100  $\mu$ m. Data are mean  $\pm$  SEM;  $n = 3$ ;  $**p < 0.01$  and  $***p < 0.001$  by one-way ANOVA with Tukey post-hoc analysis; n.s. means not significant.

linked to the SIRP $\alpha$ -CD47 axis. The phagocytosis activity of our developed CAR-Ms was significantly more potent than standard control macrophages, both in standard and inflammatory settings. Moreover, it was able to target ACs with normal or elevated expression of CD47. Given that ACs are the natural targets for macrophages, it would be worthwhile to highlight that our strategy only enhanced macrophage phagocytosis

of its target, rather than provoking phagocytosis against novel targets.

Further, we used LNPs composed of PBAP-modified  $\beta$ -CD to augment macrophage function, including efferocytosis. Anchoring the LNPs as cellular backpacks could improve the bioavailability of  $\beta$ -CD in vivo. We demonstrated this potential in a simple blood vessel-on-a-chip model, where CAR-Ms could

bind to and transmigrate into the hydrogel layer, mimicking the intima while carrying the LNPs. Previous studies have attributed the beneficial effects of these LNPs to the suppression of ROS. Indeed, oxidative stress has been shown to negatively impact cholesterol efflux and efferocytosis.

Our research has revealed that the beneficial effects of our approach are in part due to the release of HP $\beta$ -CD, which promotes metabolic reprogramming and improves LXR signaling. Previous works have shown that the LXR pathway is vital in maintaining cholesterol homeostasis and reducing inflammation. Increased catabolism by HP $\beta$ -CD released from the LNPs can reduce the overwhelming cholesterol burden caused by AC ingestion through metabolic reprogramming. Our results show that the combination of HP $\beta$ -CD and anti-CD47 CAR works synergistically to enhance phagocytosis, surpassing the effects of CD47 blockade alone. To further improve the efficacy of our approach, future work could focus on developing second or third-generation CARs with additional activation domains or linking an intracellular signaling domain to increase the release of anti-inflammatory cytokines, which could improve efferocytosis.

In conclusion, we have successfully developed a variation of CAR-M, namely CSR-M, which considerably improves macrophage phagocytic activity. Our approach is exclusively created to maximize macrophage phagocytosis of its related target, apoptotic cells. Our studies have suggested that by using LNPs composed of PBAP-modified  $\beta$ -CD, there could be an enhancement in macrophage function. Moreover, our advanced technology allows for a faster and more effective way to clear CD47Hi ACs, providing a wider clearance window and decreasing the chances of secondary necrosis in the context of atherosclerosis.

## 4. Experimental Section

**Reagents:** 4-(Hydroxymethyl)phenylboronic acid pinacol ester was purchased from Sigma-Aldrich (St. Louis, MO). Hydroxypropyl- $\beta$ -cyclodextrin (HP $\beta$ -CD) was purchased from Fisher Scientific (Waltham, MA). 1,1'-Carbonyldiimidazole was purchased from Sigma-Aldrich (St. Louis, MO). Methylene Chloride was purchased from Fisher Scientific (Waltham, MA). Dimethyl sulfoxide was purchased from Sigma-Aldrich (St. Louis, MO). 4-dimethylaminopyridine was purchased from VWR (Radnor, PA). 1,2-dimyristoyl-sn-glycero-3-phosphocholine (DMPC), 1,2-dioleoyl-sn-glycero-3-phosphate (DOPA), DSPE-PEG(2000)-maleimide (ammonium salt), and TopFluor cholesterol were purchased from Avanti Polar Lipids (Alabaster, AL). Chloroform was purchased from Fisher Scientific (Waltham, MA). Hydrogen peroxide was purchased from Sigma-Aldrich (St. Louis, MO). DCFDA was purchased from Sigma-Aldrich (St. Louis, MO). Presto Blue Cell Viability Reagent was purchased from Fisher Scientific (Waltham, MA). Nile Red was purchased from Sigma-Aldrich (St. Louis, MO). Sodium sulfate was purchased from Sigma-Aldrich (St. Louis, MO). Sodium chloride was purchased from Sigma-Aldrich (St. Louis, MO). Chloroform-D<sub>1</sub> was purchased from VWR (Radnor, PA). Potassium bromide (IR grade powder) was purchased from VWR (Radnor, PA). Cholesterol was purchased from Sigma-Aldrich (St. Louis, MO). Trypan blue 0.1% solution was purchased from VWR (Radnor, PA). BSA was purchased from Biosciences (Warrington, PA). Rutin hydrate was purchased from Sigma-Aldrich (St. Louis, MO). Protein Assay Dye Reagent Concentrate was purchased from Biorad (Hercules, CA). Sylgard 184 Silicone Elastomer was purchased from Electron Microscopy Sciences (Hatfield, PA).

**Synthesis of PBAP-CD:** Phenylboronic acid pinacol ester (PBAP) was conjugated to HP $\beta$ -CD using a previously established method.<sup>[21]</sup> Briefly, PBAP (550 mg) and CDI (760 mg) were added to 7 mL of anhydrous

DCM. The reaction flask was flushed with argon gas and stirred for 30 min at RT. The reaction mixture was washed twice with deionized water and with brine once. The organic solvent was dried using sodium sulfate, and then, vacuumed for a duration of 24 h. The PBAP-activated CDI (430 mg) was added to 9 mL of DMSO along with DMAP (270 mg) and HP $\beta$ -CD (106 mg). The reaction vessel was flushed with argon gas and stirred for 48 h at RT. The mixture was then precipitated in deionized water and collected by centrifugation. The pellet was dried under a vacuum for 24 h.

**<sup>1</sup>H-NMR and FTIR Characterization of PBAP-CD:** The PBAP-CD was characterized by proton nuclear magnetic resonance (<sup>1</sup>H-NMR) and infrared spectroscopy (IR). For <sup>1</sup>H-NMR analysis, 1 mg of PBAP-CD was dissolved in deuterated chloroform, and the sample was run on a Bruker AVANCE Neo 500 MHz NMR. For IR analysis, 1 mg of PBAP-CD was added to 100 mg of dried KBr powder. The powder was ground to a fine powder using a mortar and pestle. Approximately 50 mg of this was then used to create a KBr disc using a minipress. The spectrum was then captured using a Thermo Fisher Nicolet iS10.

**Preparation and Characterization of  $\beta$ -CD LNP:** 1,2-dimyristoyl-sn-glycero-3-phosphocholine (DMPC) and 1,2-dioleoyl-sn-glycero-3-phosphate (sodium salt) (DOPA) were constituted in 20 mM stock solutions in chloroform. The stock solutions were stored in -20 °C until use. The chloroform was vacuumed off and the lipids were redispersed in ethanol. DSPE-PEG(2000)-maleimide (ammonium salt) was reconstituted as 1 mg mL<sup>-1</sup>. DMPC (81  $\mu$ L), DOPA (51  $\mu$ L), and DSPE-PEG-maleimide (1  $\mu$ L) were added to make a 4% ethanolic solution in HEPES 7.4 pH buffer. The solution was heated at 65 °C for 1 h. PBAP-CD (5 mg) dissolved in methanol was added drop-wise to the lipid solution and vortexed for 3.75 min. The methanol was removed by evaporation for 2 h at 65 °C. The formed  $\beta$ -CD LNPs were then stored at 4 °C until use. Hydrodynamic diameter, zeta potential, and particle concentration of the  $\beta$ -CD LNPs were measured using a Malvern ZetaSizer Nano Series and NanoSight NS 3000 (Westborough, MA). For XPS analysis, 10  $\mu$ L of the  $\beta$ -CD LNP solution was dried on a cleaned silicon substrate and analyzed using a Thermo Scientific K-Alpha X-ray Photoelectron Spectrometer (XPS) System with a monochromated X-ray source (Al-K $\alpha$ ) and a base pressure of <5  $\times$  10<sup>-8</sup> mbar. TEM images of the  $\beta$ -CD LNPs were acquired using a JEOL transmission electron microscope (JEM1010; JEOL, Japan) with an accelerating voltage of 80 kV.

**$\beta$ -CD Release Kinetics from LNP:** The amount of  $\beta$ -CD released from the LNPs was determined by complexing the free  $\beta$ -CD to rutin. 4  $\mu$ L of rutin (1 mM in methanol) was added to 2 mL  $\beta$ -CD LNPs (1 mg mL<sup>-1</sup> in HEPES 7.4 buffer). The sample was aliquoted into 300  $\mu$ L portions, followed by adding H<sub>2</sub>O<sub>2</sub> (10 mM stock). The sample was then pipetted into a 96 well plate at 100  $\mu$ L per well. The fluorescence was measured at various time points using a microplate reader. The calibration curve was generated by adding 100  $\mu$ L rutin hydrate at various concentrations (0, 2, 4, 6, and 8 mM) along with  $\beta$ -CD as previously described.<sup>[46]</sup> The calibration curve was measured and determined individually for each time point. The same protocol was repeated with some minor changes to facilitate total hydrolysis. The  $\beta$ -CD LNPs were aliquoted, followed by the addition of 1 mM H<sub>2</sub>O<sub>2</sub>. The sample was incubated at RT overnight. Rutin was then added, incubated for 30 min, and fluorescence measured.

**Cell Culture:** The human monocytic cell line THP-1 cells were cultured in complete RPMI-1640 medium (Gibco, Thermo Fisher Scientific) with 10% FBS, 1% penicillin-streptomycin, and 0.1%  $\beta$ -mercaptoethanol. The THP-1 cells were differentiated into macrophage-like cells with 50 ng mL<sup>-1</sup> phorbol 12-myristate 13-acetate (PMA) (Tocris Bioscience) for 48 h. For polarization into M1-like macrophages, the cells were incubated with 100 ng mL<sup>-1</sup> LPS and 50 ng mL<sup>-1</sup> IFN- $\gamma$  for 24 h after differentiation. HEK293 and MCF-7 cells were cultured as Dulbecco's modified Eagle's medium (DMEM) supplemented with 10% FBS, 1% penicillin-streptomycin, 1% non-essential amino acids (NEAA), and L-glutamine. HUVECs were cultured in endothelial growth medium (DMEM/F12, 2% FBS, 1  $\mu$ g mL<sup>-1</sup> hydrocortisone, 5 ng mL<sup>-1</sup> EGF, 10 ng mL<sup>-1</sup> FGF-2, 20  $\mu$ g mL<sup>-1</sup> heparin sulphate, 250 ng mL<sup>-1</sup> insulin, and 100 U mL<sup>-1</sup> penicillin). The cells were cultured at 37 °C in a humidified atmosphere containing 5% CO<sub>2</sub>.

**ROS Scavenging Assay:** UV-induced photodegradation of rhodamine B was used to examine the ROS-scavenging effect of  $\beta$ -CD. Briefly, 1.68 mM of  $H_2O_2$  was subjected to UV-irradiation for 1 h; then, mixed with rhodamine B with a final rhodamine B concentration of 10  $\mu$ M. The mixture (with and without LNPs) was further irradiated for 15–20 min, and the absorbance of rhodamine B was recorded at 553 nm using a Varian Cary50 spectrophotometer.

For intracellular ROS measurement, THP-1 cells were seeded at 30 000 cells per well and differentiated for 48 h. Thereafter, the media was replaced with serum-free media and the cells were incubated with 50  $\mu$ M  $H_2O_2$  in addition to varying doses of  $\beta$ -CD LNPs for 1 h at 37 °C. The cells were then washed twice with PBS and incubated with 2'-7'-Dichlorodihydrofluorescein diacetate DCFDA (100  $\mu$ M) for 2 h at 37 °C. Fluorescence was then measured (excitation 485 nm, emission 535 nm). The amount of ROS scavenged was determined by plotting a calibration curve with the negative and positive control.

**Cell Viability:** Cell viability was measured by incubating macrophages with  $\beta$ -CD LNP at varying concentrations for 24 h. The Presto Blue assay (10% volume ratio to cell medium; Thermo Fisher Scientific) was then carried out according to the manufacturer's instructions. A calibration plot was also plotted using positive and negative control. The concentration of  $\beta$ -CD LNP refers to the concentration of  $\beta$ -CD assuming 100% encapsulation.

**Cholesterol Crystal Preparation and Dissolution:** Cholesterol monohydrate crystals were prepared as reported previously.<sup>[41]</sup> Briefly, cholesterol was dissolved in hot acetone at 20 mg mL<sup>-1</sup>. The opaque solution was heated to 90 °C to dissolve, followed by precipitation in an ice bath. This cycle was repeated six times. In the last cycle, nuclease-free water was added to 10% of the final volume to create monohydrate cholesterol crystals (CC). The CC were collected by centrifugation, and the acetone/water mixture was decanted. The dried crystals were further reduced in size using a probe ultrasonicator (20 kHz, 5 Watts) in sterile, tissue grade PBS for 1 h on ice. For fluorescently labeled CC, a small amount of BODIPY-labeled cholesterol (TopFluor-cholesterol, Avanti, Alabaster, AL) was doped into the cholesterol solution in acetone. The capacity of  $\beta$ -CD LNPs to dissolve CC was evaluated by incubating different concentrations of LNPs with CC at a fixed  $H_2O_2$  concentration for 16 h at 37 °C. The samples were subsequently filtered with a 0.22  $\mu$ m filter and supernatant (filtrate) collected for fluorescence analysis using a Tecan microplate reader (Mannedorf, Switzerland) using an excitation wavelength of 488 nm and emission wavelength of 550 nm. The crystalline fraction was obtained by incubating the filters with hot methanol, and the fluorescence was recorded.

**Intracellular CC Content:** Macrophages were incubated with 2  $\mu$ g of CC for 3 h, followed by treatment with  $\beta$ -CD LNPs for 24 h. The cells were washed three times with PBS, once with 0.1% Trypan Blue solution, followed by three times with PBS. The absorbance of the BODIPY-cholesterol was then measured.

**Foamy Macrophage Staining:** To evaluate the capability of  $\beta$ -CD LNP-backpacked macrophages to resist lipid accumulation, Nile Red staining was employed. In short, LNP-backpacked THP-1 cells were seeded at 30 000 cells per well in a 96-well plate and differentiated with PMA. After differentiation, the cells were incubated with PBS or ox-LDL (25  $\mu$ g mL<sup>-1</sup>) for 24 h in serum-free media, followed by the addition of an equal volume of media with FBS for another 24 h. The cells were then washed, fixed, and stained with 5  $\mu$ L of 1 mg mL<sup>-1</sup> Nile Red for 30 min at RT. The cells were subsequently washed twice, and fluorescence was recorded using a Tecan microplate reader (excitation 488, emission 550).

**Quantitative Reverse Transcription Polymerase Chain Reaction (RT-qPCR):** Depending on the experiments, the total RNA was isolated from cells, either 9 or 24 h-post incubation for CC-related studies and efferocytosis experiments, respectively, using TRIzol Reagent (LifeTechnologies, MA). The total RNA was reverse transcribed to cDNA using SuperScriptIII First-Strand Synthesis System (LifeTechnologies, MA). The cDNA used for qPCR reactions was performed using a StepOnePlus RT-PCR system (Applied Biosystems) with Power SYBR Green PCR master mix (Applied Biosystems). The gene expression levels were reported in fold change values relative to control and normalized against glyceraldehyde-3-phosphate

**Table 1.** The primers used in this study.

Gene	Forward primer	Reverse primer
GAPDH	CATGTTCCAATATGATTCCACC	GATGGATTCCATTGATGAC
IL-1 $\beta$	ATGATGGCTTATTACAGTGCCAA	GTCGGAGATTCTAGTCTGGA
IL-6	AAACAACCTGAACCTTCCAAGA	GCAAGTCTCCTATTGAATCCA
ABCA1	ACATCTGAAGCCAATCCTGA	CTCCTGTCGATGCTACTCC
ABCG1	ATTACAGGACCTTTCCTATTCCG	CTCACCCTATTGAACCTCCCG
CYP27A1	CGGCAACGGAGCTTAGAGG	GGCATAGCCTTGAACGAACAG
IL-10	GCTCCTGAGGTATGGAATAGAGTCC	TATGTGTCAATTTGCGGGGGC
MERTK	CTCTGGCGTAGAGCTATCACT	AGGCTGGTGGTGAAACA
CD206	CTACAAGGGATCGGGTTTATGGA	TTGGCATTGCTAGTAGCGTA
TFEB	ACCTGTCGAGACCTATGGG	CGTCCAGACGATAATGTTGTC
CCL2	CAGCCAGATGCAATCAATGCC	CAGCCAGATGCAATCAATGCC
NLRP3	CCACAAGATCGTGAGAAAACCC	CGGTCCTATGTCTCGTCA
TNF- $\alpha$	CTGCTGCACCTTTGGAGTGAT	AGATGATCTGACTGCCTGGG

dehydrogenase (GAPDH) gene expression. The primers are listed in **Table 1**.

**Antibody Coupling to  $\beta$ -CD LNP:** Anti-CD45 antibodies were conjugated to the LNPs using thiol-maleimide coupling as reported in literature.<sup>[42]</sup> For a typical reaction, 10  $\mu$ g of anti-human CD45 antibody (BioLegend, San Diego, CA) reconstituted in a small volume of PBS containing 2 mM EDTA at pH 7.4 was activated using Traut's reagent for 1 h at RT. Subsequently, 900  $\mu$ L of LNPs was added, and the solution was left on a rotatory shaker for 16 h at 4 °C. Following the reaction, 1  $\mu$ M L-cysteine was added to quench any unreacted maleimide groups. Unreacted mAbs were purified with Vivaspin 500 (Sartorius, Gotten, Germany). The antibody-coupled LNPs were stored at 4 °C until use. The concentration of the antibody on the surface of the LNPs was determined by the Bradford assay and the absorbance measured at 595 nm. A calibration curve was determined using BSA (Polysciences, Warrington PA).

**Backpacking of  $\beta$ -CD LNPs to THP-1 Cells:** The  $\beta$ -CD LNP backpacks were loaded onto the cells using a modified procedure as described previously.<sup>[22]</sup> For a typical experiment,  $1.0 \times 10^6$  cells were incubated with 90  $\mu$ L of the LNPs in Hank's Balanced Salt Solution (HBSS) (Gibco, Thermo Fisher Scientific) for 1 h at 37 °C. Thereafter, the cells were washed three times with HBSS and used for subsequent experiments. The loading efficiency at different concentrations was calculated by the following formula:

$$\text{Loading Efficiency (LE\%)} = (1 - Cf/Ct) \times 100\% \quad (1)$$

where Cf is the fluorescence of the amount of free, non-loaded LNP in the supernatant and Ct is the fluorescence of the total amount of LNPs. To determine dose-dependent loading, various concentrations of LNPs were incubated with  $1.0 \times 10^6$  cells, washed three times, and analyzed by flow cytometry using a Beckman Coulter Gallios Cytometer (Beckman Coulter, Brea, California), equipped with 405, 488, and 638 nm lasers. Data were analyzed using Beckman Coulter Kaluza version 1.2 software. To visualize the LNPs on the THP-1 cells, the backpacked cells in suspension were labeled with CMTPIX (C<sub>4</sub>H<sub>40</sub>ClN<sub>3</sub>O<sub>4</sub>; Invitrogen), washed, and adhered onto the glass coverslips using a previously described method.<sup>[30]</sup> The macrophages were fixed and imaged using a Zeiss LSM800 confocal microscope.

**Surface Imaging and Quantification of  $\beta$ -CD LNPs:** Characterization of CAR-Ms backpacked with  $\beta$ -CD LNPs was conducted using field emission scanning electron microscopy (FE-SEM). To prepare the sample,  $5 \times 10^4$  cells were differentiated on a 10 mm  $\times$  10 mm size of glass substrate and cultured for 2 days. The cells were washed three times with DPBS and fixed using 4% formaldehyde in DPBS for 10 min at RT. The fixed cells were subjected to graded dehydration using various concentrations

of ethanol (30%, 50%, 70%, 90%, and 100%, each for 10 min) and hexamethyldisilazane (HMDS) (50% and 100%, each for 10 min). The dehydrated cells were air-dried overnight on a clean bench. Afterward, the glass with the dried cells was mounted onto aluminum stubs and coated with 20 nm of gold using a sputter coater. The morphology of the CAR-Ms with  $\beta$ -CD LNPs was then observed using FE-SEM (10 kV, Carl Zeiss, Germany). The images obtained from FE-SEM were analyzed for morphological changes due to the  $\beta$ -CD LNPs. CAR-Ms and  $\beta$ -CD LNP backpacks in the FE-SEM image were pseudocolored using Adobe photoshop. To quantify surface-coupled  $\beta$ -CD LNPs, DSPE-PEG-biotin was incorporated into the LNPs via post-insertion for 15 min at 55 °C.<sup>[43]</sup> The purified antibody-coupled LNPs were prepared and conjugated to the cell surface as described in the above section. Surface detection of LNPs was achieved by staining the cells with streptavidin-AlexaFluor 647 and detection by flow cytometry.

**Lentiviral Vector Design and Production:** The humanized anti-CD47 scFv was designed based on previous work for engineering anti-CD47 CAR T-cells.<sup>[44]</sup> The lentiviral expression vector was custom cloned by VectorBuilder. For lentivirus production, HEK293T cells were cultured to 60–70% confluency before transfecting with the expression vector, the psPAX2 packaging vector (Addgene #12260), and the envelope vector pMD2.G (Addgene #12259) at a ratio of 4:3:1, respectively, using Lipofectamine 3000. The supernatant containing lentiviral particles was harvested 48–72 h post-transfection and filtered with a 0.45  $\mu$ m syringe filter, and the virus was isolated using the PEG6000 precipitation method as reported.<sup>[45]</sup> Lentivirus titer was determined using the qPCR Lentivirus Titer Kit (Applied Biological Materials, Canada) according to the manufacturer's instruction.

**Transduction and Selection of THP-1 Cells by FACS:** THP-1 cells ( $1.0 \times 10^5$  cells) were transduced with lentivirus at various multiplicities of infection (MOI), ranging from 0.5 to 20. Successfully transduced cells were expanded and sorted by FACS using the MoFlo Astrios cell sorter (Beckman Coulter, Brea, California).

**Detection of Surface CAR by Protein L:** The detection and quantification of CAR on THP-1 cells were performed using Protein L as described previously.<sup>[35]</sup> In short,  $1.0 \times 10^6$  cells were washed three times with 1 $\times$  PBS and resuspended in 0.5 mL of FACS buffer (1 $\times$  PBS, 25 mM HEPES, 1% FBS). The cells were stained with 1  $\mu$ g of biotinylated protein L (GenScript, Piscataway, NJ) for 45 min at 4 °C. The cells were subsequently washed three times with ice-cold buffer; then, stained with AlexaFluor 647-streptavidin for 30 min at 4 °C. The cells were analyzed by flow cytometry as described above.

**CD47 Bead Preparation and Phagocytosis Assay:** Liposome-coated beads containing CD47 mimicking CD47-rich apoptotic bodies were prepared using a previously described method with some modifications.<sup>[18c]</sup> Small unilamellar vesicles (SUVs) containing 95% DMPC, 2% Ni2+-DGS-NTA, 0.5% PEG5000-PE, and 0.5% Liss Rhod-PE were prepared using the thin film hydration method, sonicated, and cleared by 33 freeze thaw cycles. Silica microbeads (3  $\mu$ m in size; Bangs Labs, IN) were mixed with the SUVs at a 2 mM final concentration for 30 min at RT on a rotary shaker in the dark. The liposome-coated beads were washed twice with PBS, resuspended in PBS + 0.1% w/v BSA, and incubated with recombinant human CD47-his (Sino Biological) for an additional 45 min. The CD47-coupled beads were further washed twice with PBS and resuspended in PBS + 0.1% w/v BSA. For phagocytosis assays, control macrophages and CAR-M were incubated with the beads for 2 h at 37 °C, washed three times with PBS, fixed with 4% formaldehyde, and stained with anti-CD11b antibody (control) or anti-GFP antibody (CAR-M) prior to imaging with a Zeiss LSM800 confocal microscope. The internalized beads were quantified using ImageJ.

**Generating CD47Hi ACs and Standard ACs:** MCF7 cells ( $1.0 \times 10^5$  cells) were seeded into a 24-well plate and stimulated with TNF- $\alpha$  at 50 ng mL<sup>-1</sup> for 48 h. The cells were then treated with 1  $\mu$ M of staurosporine (STS) for 4 h. The expression of CD47 was confirmed by flow cytometry and fluorescence microscopy. For standard AC preparation, Jurkat cells ( $2.0 \times 10^6$  cells) in PBS were seeded into a 6 cm dish and irradiated under a UV lamp for 5 min. The cells were redispersed in growth media and cultured for another 2–4 h prior to further experimentation.

**Phagocytosis of ACs and Quantification by CellTagging:** Control (untransduced) THP-1 cells or CAR-expressing THP-1 cells were seeded at  $1.0 \times 10^5$  cells per well in a 48-well plate and differentiated with 50 ng mL<sup>-1</sup> PMA for 48 h. CMTPIX-labeled CD47<sup>Hi</sup> MCF7 ACs were fed to the phagocytes at a ratio of 3 AC: 1 macrophage for 2 h at 37 °C. Subsequently, the media were gently aspirated off and the wells washed with warm PBS three times to remove any unbound ACs. The macrophages were fixed and stained with anti-CD11b antibody (control) or anti-GFP antibody (CAR-M). The macrophages (at least 50 phagocytes per field) in four to five field of views were imaged using either a ZOE Fluorescent Cell Imager or a Zeiss LSM800 confocal microscope. For time-lapse imaging, a Nikon Eclipse Ti-E microscope was used to image the macrophages incubated with ACs for a total duration of 1 h. To further distinguish the proportion of cells that were partially engulfed or completely engulfed, the proportion of fluorescent-positive cells was calculated using an automated method run with python slightly modified from the CellTagging Script developed by Guo et al.<sup>[39]</sup> Briefly, the background image was translated into binary images by thresholding the green fluorescent signal. The Otsu method was utilized to determine the threshold for detecting green fluorescence. The watershed method was used to segment the binary image into individual cells. The detected cells were then filtered to remove cell aggregates and debris. The intensity of the red fluorescent signal of interest was then quantified to determine the colocalization of green and red fluorescent signal, as well as the percentage of cells with fluorescence to cells with minimal fluorescent signals to cells with no red fluorescence based on set thresholds in the processed image. The processes were run with the Python 3.11.1 and its libraries: scikit-image 0.19.2, numpy 1.24.0, matplotlib 3.6.2, seaborn 0.12.2, and jupyter 5.2.

**Activation of HUVECs:** Stimulation of HUVECS was achieved by treating the cells with TNF- $\alpha$  at a concentration ranging from 0 to 10 ng mL<sup>-1</sup> for at least 24 h at 37 °C. The cells in four to five view fields were imaged using a ZOE Fluorescent Cell Imager and fluorescence analyzed by ImageJ.

**Cytotoxicity of CAR-M:** The day prior to the experiment,  $3.0 \times 10^5$  HUVECs were seeded into a six well plate. An equal volume of  $3.0 \times 10^5$  control macrophages or CAR-Ms in complete RPMI media (800  $\mu$ L) were added to the HUVECs. To test the toxicity of CD47-blockade, HUVECs were pre-treated with 10  $\mu$ g mL<sup>-1</sup> of CD47 antibodies for 30 min prior to the addition of macrophages. The cells were co-cultured for 24 h at 37 °C and analyzed by flow cytometry. Toxicity was measured by calculating the percentage of cells positive for 4',6-diamidino-2-phenylindole (DAPI) and CD31.

**Fabrication of the Microfluidic Device:** The microfluidic device was fabricated using Poly(dimethylsiloxane) (PDMS, Sylgard 184, Dow Corning, USA) and mold printed with polycaprolactone (PCL) filaments. The microfluidic model was designed in Sketchup (Google, Inc., Mountain View, CA), exported as STL files, and translated into a printable g-code file using Perfactory Rapid Prototype (RP) (EnvisionTEC, Inc., Dearborn, MI). The g-code was exported to the 3D Bioplotter where it was assigned the material file for polycaprolactone (PCL) (Lot MKCL2159, avg Mn 45k). PCL was loaded into the high-temperature cartridge fitted with a 24 G, 4 mm in length, stainless steel luer lock needle. PCL was printed at a temperature of 125 °C and 6 bar pressure at a speed of 1 mm s<sup>-1</sup> at a 37 °C build plate on a plastic 10 cm petri dish. PDMS secondary templates were prepared using this PCL master by pouring a PDMS prepolymer-catalyst mixture onto the 3D printed structure and cured at a low temperature (37 °C) for 24 h to prevent the melting of PCL. The PDMS cast was then attached to a clean glass slide by plasma treatment at 70 W for 2.05 min (CUTE, Femto Science Inc., Korea). The polar silanol groups on the plasma-treated surfaces of both materials formed irreversible bonds, allowing the assembled device to withstand high pressure.

**Macrophage Penetration/Migration in Different GelMA Concentrations:** 5%, 6.5%, 7.5%, and 10% GelMA solutions w/v were prepared in complete macrophage media in the presence of  $1 \times 10^6$  apoptotic cells per mL and 0.5% Irgacure w/v. GelMA hydrogels were obtained after cross-linking under UV (312 nm, at a 3 cm distance), washed with PBS, and incubated O/N with  $1.0 \times 10^6$  CAR-Ms per mL or  $2.0 \times 10^6$  CAR-Ms loaded with LNPs per mL. Hydrogels prepared without ACs were used as control. The next day, the hydrogels were washed with PBS twice and transferred into a new 96 well plate containing PBS to observe under a fluorescence microscope.

Received: August 17, 2023  
Revised: February 5, 2024  
Published online: February 22, 2024

**Microfluidic Culturing of HUVEC and Transmigration of THP-1 Macrophages:** The GelMA layer of the model was formed in the microfluidic device by injecting uncross-linked 6.5% w/v GelMA with 0.5% w/v Irgacure, 0.75  $\mu\text{g mL}^{-1}$  of  $\text{CCl}_2$ , and  $2.0 \times 10^6$  ACs  $\text{mL}^{-1}$  to the shallower channel. Then, the GelMA was cross-linked under UV treatment for 1 min. After cross-linking, Tris-HCL buffer containing 0.5  $\text{mg mL}^{-1}$  of dopamine hydrochloride (Sigma-Aldrich, USA) was injected into the deeper channel to incubate cross-linked GelMA for 45 min. The dopamine coating promoted the attachment of HUVECs on the surfaces of GelMA. Subsequently, PBS was used to wash the residual dopamine from the non-GelMA surfaces. HUVECs were then seeded in the deeper channel ( $2.0 \times 10^6$  cells  $\text{mL}^{-1}$ ). Seeded HUVECs were incubated at 37 °C until the complete coverage of the GelMA layer with daily media change. The layer of HUVECs was activated by adding media with 1  $\text{ng mL}^{-1}$  of TNF- $\alpha$ . 24 h after the activation, macrophages stained with CMTPIX were injected into the shallower channel and incubated overnight. The next day, unattached macrophages were washed away twice with PBS. The extent of trans-migration of the macrophages into the GelMA layer was studied using Zeiss LSM710 (Oberkochen, Germany) confocal laser scanning electron microscope, and the images were analyzed using NIH Image J.

**Statistical Analysis:** All statistical analysis was performed in Prism 9.5.0 (GraphPad, Inc.). The statistical test used is indicated in each figure legend. Error bars throughout the paper denote 95% confidence intervals of the mean.

## Supporting Information

Supporting Information is available from the Wiley Online Library or from the author.

## Acknowledgements

S.T.C. and J.B.S. contributed equally to this work. K-B.L. acknowledges the partial financial support from the NSF (CBET-1803517), the New Jersey Commission on Spinal Cord Research (CSCR17IRG010; CSCR16ERG019), NIH R21 (R21AR071101) and NIH R01 (1R01DC016612, 3R01DC016612-01S1, and 5R01DC016612-02S1), the Alzheimer's Association (CSCR22ERG023), N.J. Commission on Cancer Research (COCR23PPR007), and the National Heart, Lung, and Blood Institute (NHLBI, U01HL150852). S.T.C. and S.N. acknowledge fellowship support as part of the NIH T32 Biotechnology Training Program (GM135141) and H.K.C. appreciates the fellowship of the NIH T32 Postdoctoral Training Program in Translational Research in Regenerative Medicine, under Award Number T32EB005583. Flow cytometry was performed by the Cytometry/Cell Sorting Core Facility at EOHSI, Rutgers University. Core operations are supported by grants from the National Institutes of Health Grants P30ES005022 and S10OD026876. The authors are grateful to Yannan Hou for the generous help with XPS analysis.

## Conflict of Interest

The authors declare no conflict of interest.

## Data Availability Statement

The data that support the findings of this study are available from the corresponding author upon reasonable request.

## Keywords

atherosclerosis,  $\beta$ -cyclodextrin, CAR macrophage, efferocytosis, lipid nanoparticle

- [1] a) M. P. Chao, R. Majeti, I. L. Weissman, *Nat. Rev. Cancer* **2012**, *12*, 58; b) M. Feng, K. D. Marjon, F. Zhu, R. Weissman-Tsakamoto, A. Levett, K. Sullivan, K. S. Kao, M. Markovic, P. A. Bump, H. M. Jackson, T. S. Choi, J. Chen, A. M. Banuelos, J. Liu, P. Gip, L. Cheng, D. Wang, I. L. Weissman, *Nat. Commun.* **2018**, *9*, 3194.
- [2] R. E. Voll, M. Herrmann, E. A. Roth, C. Stach, J. R. Kalden, I. Girkontaite, *Nature* **1997**, *390*, 350.
- [3] Y. Kojima, J. P. Volkmer, K. McKenna, M. Civelek, A. J. Lusis, C. L. Miller, D. Direnzo, V. Nanda, J. Ye, A. J. Connolly, E. E. Schadt, T. Quertermous, P. Betancur, L. Maegdefessel, L. P. Matic, U. Hedin, I. L. Weissman, N. J. Leeper, *Nature* **2016**, *536*, 86.
- [4] R. Stocker, J. F. Keane Jr., *Physiol. Rev.* **2004**, *84*, 1381.
- [5] a) P. Duewell, H. Kono, K. J. Rayner, C. M. Sirois, G. Vladimer, F. G. Bauernfeind, G. S. Abela, L. Franchi, G. Nuñez, M. Schnurr, T. Espevik, E. Lien, K. A. Fitzgerald, K. L. Rock, K. J. Moore, S. D. Wright, V. Hornung, E. Latz, *Nature* **2010**, *464*, 1357; b) K. Rajamäki, J. Lappalainen, K. Oörni, E. Välimäki, S. Matikainen, P. T. Kovanen, K. K. Eklund, *PLoS One* **2010**, *5*, 11765.
- [6] A. M. Flores, N. Hosseini-Nassab, K.-U. Jarr, J. Ye, X. Zhu, R. Wirka, A. L. Koh, P. Tsantilis, Y. Wang, V. Nanda, Y. Kojima, Y. Zeng, M. Lotfi, R. Sinclair, I. L. Weissman, E. Ingelsson, B. R. Smith, N. J. Leeper, *Nat. Nanotechnol.* **2020**, *15*, 154.
- [7] a) I. G. Schulman, *FEBS Lett.* **2017**, *591*, 2978; b) C. Yin, B. Heit, *Front. Immunol.* **2021**, *12*, 631714; c) H. Z. Ford, L. Zeboudj, G. S. D. Purvis, A. Ten Bokum, A. E. Zarebski, J. A. Bull, H. M. Byrne, M. R. Myerscough, D. R. Greaves, *Proc. Biol. Sci.* **2019**, *286*, 20190730.
- [8] C. W. Tsao, A. W. Aday, Z. I. Almarzooq, A. Alonso, A. Z. Beaton, M. S. Bittencourt, A. K. Boehme, A. E. Buxton, A. P. Carson, Y. Commodore-Mensah, M. S. V. Elkind, K. R. Evenson, C. Eze-Nliam, J. F. Ferguson, G. Generoso, J. E. Ho, R. Kalani, S. S. Khan, B. M. Kissela, K. L. Knutson, D. A. Levine, T. T. Lewis, J. Liu, M. S. Loop, J. Ma, M. E. Mussolino, S. D. Navaneethan, A. M. Perak, R. Poudel, M. Rezk-Hanna, et al., *Circulation* **2022**, *145*, e153.
- [9] I. Zanotti, F. Potì, M. Pedrelli, E. Favari, E. Molero, G. Franceschini, L. Calabresi, F. Bernini, *J. Lipid Res.* **2008**, *49*, 954.
- [10] A. G. N., S. J. Bensinger, C. Hong, S. Beceiro, M. N. Bradley, N. Zelcer, J. Deniz, C. Ramirez, M. Díaz, G. Gallardo, C. R. de Galarreta, J. Salazar, F. Lopez, P. Edwards, J. Parks, M. Andujar, P. Tontonoz, A. Castriello, *Immunity* **2009**, *31*, 245.
- [11] a) C. Hong, R. Walczak, H. Dhamko, M. N. Bradley, C. Marathe, R. Boyadjian, J. V. Salazar, P. Tontonoz, *J. Lipid Res.* **2011**, *52*, 531; b) A. Viola, F. Munari, R. Sánchez-Rodríguez, T. Scolaro, A. Castegna, *Front. Immunol.* **2019**, *10*, 1462.
- [12] M. B. Fessler, *Pharmacol. Ther.* **2018**, *181*, 1.
- [13] S. Zimmer, A. Grebe, S. S. Bakke, N. Bode, B. Halvorsen, T. Ulas, M. Skjelland, D. De Nardo, L. I. Labzin, A. Kersiek, C. Hempel, M. T. Heneka, V. Hawhurst, M. L. Fitzgerald, J. Trebicka, I. Björkhem, J. Gustafsson, M. Westerterp, A. R. Tall, S. D. Wright, T. Espevik, J. L. Schultze, G. Nickenig, D. Lütjohann, E. Latz, *Sci. Transl. Med.* **2016**, *8*, 333ra50.
- [14] a) M. A. Crumling, K. A. King, R. K. Duncan, *Front. Cell. Neurosci.* **2017**, *11*, 355; b) C. D. Davidson, Y. I. Fishman, I. Puskás, J. Szemán, T. Sohajda, L. A. McCauliff, J. Sikora, J. Storch, M. T. Vanier, L. Szente, S. U. Walkley, K. Dobrenis, *Ann. Clin. Transl. Neurol.* **2016**, *3*, 366.
- [15] a) Y. Wang, L. Li, W. Zhao, Y. Dou, H. An, H. Tao, X. Xu, Y. Jia, S. Lu, J. Zhang, H. Hu, *ACS Nano* **2018**, *12*, 8943; b) H. Kim, S. Kumar, D. W. Kang, H. Jo, J. H. Park, *ACS Nano* **2020**, *14*, 6519; c) Y. Zhang, F.

- Gong, Y. Wu, S. Hou, L. Xue, Z. Su, C. Zhang, *Nano Lett.* **2021**, *21*, 9736.
- [16] a) K. C. Pehlivan, B. B. Duncan, D. W. Lee, *Curr. Hematol. Malig. Rep.* **2018**, *13*, 396; b) S. A. Grupp, M. Kalos, D. Barrett, R. Aplenc, D. L. Porter, S. R. Rheingold, D. T. Teachey, A. Chew, B. Hauck, J. F. Wright, M. C. Milone, B. L. Levine, C. H. June, *N. Engl. J. Med.* **2013**, *368*, 1509.
- [17] a) H. Aghajanian, T. Kimura, J. G. Rurik, A. S. Hancock, M. S. Leibowitz, L. Li, J. Scholler, J. Monslow, A. Lo, W. Han, T. Wang, K. Bedi, M. P. Morley, R. A. Linares Saldana, N. A. Bolar, K. McDaid, C. A. Assenmacher, C. L. Smith, D. Wirth, C. H. June, K. B. Margulies, R. Jain, E. Puré, S. M. Albelda, J. A. Epstein, *Nature* **2019**, *573*, 430; b) C. Amor, J. Feucht, J. Leibold, Y.-J. Ho, C. Zhu, D. Alonso-Curbelo, J. Mansilla-Soto, J. A. Boyer, X. Li, T. Giavridis, A. Kulick, S. Houlihan, E. Peersckhe, S. L. Friedman, V. Ponomarev, A. Piersigilli, M. Sadelain, S. W. Lowe, *Nature* **2020**, *583*, 127; c) C. R. Maldini, D. T. Claiborne, K. Okawa, T. Chen, D. L. Dopkin, X. Shan, K. A. Power, R. T. Trifonova, K. Krupp, M. Phelps, V. D. Vrbanac, S. Tanno, T. Bateson, G. J. Leslie, J. A. Hoxie, C. L. Boutwell, J. L. Riley, T. M. Allen, *Nat. Med.* **2020**, *26*, 1776.
- [18] a) G. Xie, H. Dong, Y. Liang, J. D. Ham, R. Rizwan, J. Chen, *EBioMedicine* **2020**, *59*, 102975; b) M. Klichinsky, M. Ruella, O. Shestova, X. M. Lu, A. Best, M. Zeeman, M. Schmierer, K. Gabrusiewicz, N. R. Anderson, N. E. Petty, K. D. Cummins, F. Shen, X. Shan, K. Veliz, K. Blouch, Y. Yashiro-Ohtani, S. S. Kenderian, M. Y. Kim, R. S. O'Connor, S. R. Wallace, M. S. Kozlowski, D. M. Marchione, M. Shestov, B. A. Garcia, C. H. June, S. Gill, *Nat. Biotechnol.* **2020**, *38*, 947; c) M. A. Morrissey, A. P. Williamson, A. M. Steinbach, E. W. Roberts, N. Kern, M. B. Headley, R. D. Vale, *Elife* **2018**, *7*, 36688; d) M. Kang, S. H. Lee, M. Kwon, J. Byun, D. Kim, C. Kim, S. Koo, S. P. Kwon, S. Moon, M. Jung, J. Hong, S. Go, S. Y. Song, J. H. Choi, T. Hyeon, Y. K. Oh, H. H. Park, B. S. Kim, *Adv. Mater.* **2021**, *33*, 2103258; e) C. Chen, W. Jing, Y. Chen, G. Wang, M. Abdalla, L. Gao, M. Han, C. Shi, A. Li, P. Sun, X. Jiang, Z. Yang, S. Zhang, J. Zhang, C. Tang, Y. Liu, R. Zhang, F. Xu, B. Dong, X. Li, M. Liu, B. Qiang, Y. Sun, X. Wei, J. Li, Q. Hu, X. Jiang, *Sci. Transl. Med.* **2022**, *14*, eabn1128.
- [19] S. Zhang, S. Weinberg, M. DeBerge, A. Gainullina, M. Schipma, J. M. Kinchen, I. Ben-Sahra, D. R. Gius, L. Yvan-Charvet, N. S. Chandel, P. T. Schumacker, E. B. Thorp, *Cell Metab.* **2019**, *29*, 443.
- [20] a) M. T. Stephan, J. J. Moon, S. H. Um, A. Bershteyn, D. J. Irvine, *Nat. Med.* **2010**, *16*, 1035; b) C. W. t. Shields, M. A. Evans, L. L. Wang, N. Baugh, S. Iyer, D. Wu, Z. Zhao, A. Pusuluri, A. Ukidve, D. C. Pan, S. Mitragotri, *Sci. Adv.* **2020**, *6*, eaaz6579; c) S. Prakash, N. Kumbhojkar, J. R. Clegg, S. Mitragotri, *Curr. Opin. Colloid Interface Sci.* **2021**, *52*, 101408.
- [21] Y. Zheng, L. Tang, L. Mabardi, S. Kumari, D. J. Irvine, *ACS Nano* **2017**, *11*, 3089.
- [22] L. Tang, Y. Zheng, M. B. Melo, L. Mabardi, A. P. Castaño, Y. Q. Xie, N. Li, S. B. Kudchodkar, H. C. Wong, E. K. Jeng, M. V. Maus, D. J. Irvine, *Nat. Biotechnol.* **2018**, *36*, 707.
- [23] R. Tenchov, R. Bird, A. E. Curtze, Q. Zhou, *ACS Nano* **2021**, *15*, 16982.
- [24] Y. Wang, L. Li, W. Zhao, Y. Dou, H. An, H. Tao, X. Xu, Y. Jia, S. Lu, J. Zhang, *ACS Nano* **2018**, *12*, 8943.
- [25] A. C. Calkin, P. Tontonoz, *Arterioscler., Thromb., Vasc. Biol.* **2010**, *30*, 1513.
- [26] D. Zhang, Y. Wei, K. Chen, X. Zhang, X. Xu, Q. Shi, S. Han, X. Chen, H. Gong, X. Li, J. Zhang, *Adv. Healthcare Mater.* **2015**, *4*, 69.
- [27] J. Yuan, L. Li, Q. Yang, H. Ran, J. Wang, K. Hu, W. Pu, J. Huang, L. Wen, L. Zhou, Y. Jiang, X. Xiong, J. Zhang, Z. Zhou, *ACS Nano* **2021**, *15*, 16076.
- [28] a) A. C. Marques, P. J. Costa, S. Velho, M. H. Amaral, *J. Controlled Release* **2020**, *320*, 180; b) L. Martínez-Jothar, S. Doukeridou, R. M. Schifferers, J. Sastre Torano, S. Oliveira, C. F. van Nostrum, W. E. Hennink, *J. Controlled Release* **2018**, *282*, 101.
- [29] M. Im, H. Chae, T. Kim, H. H. Park, J. Lim, E. J. Oh, Y. Kim, Y. J. Park, K. Han, *Korean J. Lab. Med.* **2011**, *31*, 148.
- [30] M. Tsang, J. Gantchev, F. M. Ghazawi, I. V. Litvinov, *BioTechniques* **2017**, *63*, 230.
- [31] a) A. Singhal, L. Szente, J. E. K. Hildreth, B. Song, *Cell Death Dis.* **2018**, *9*, 1019; b) A. Singhal, E. S. Krystofiak, W. G. Jerome, B. Song, *Sci. Rep.* **2020**, *10*, 8663.
- [32] J. H. Madenspacher, E. D. Morrell, K. M. Gowdy, J. G. McDonald, B. M. Thompson, G. Muse, J. Martinez, S. Thomas, C. Mikacenic, J. A. Nick, E. Abraham, S. Garantziotis, R. D. Stapleton, J. M. Meacham, M. J. Thomassen, W. J. Janssen, D. N. Cook, M. M. Wurfel, M. B. Fessler, *JCI Insight* **2020**, *5*, 137189.
- [33] M. Viaud, S. Ivanov, N. Vujic, M. Duta-Mare, L. E. Aira, T. Barouillet, E. Garcia, F. Orange, I. Dugail, I. Hainault, C. Stehlik, S. Marchetti, L. Boyer, R. Guinamard, F. Foufelle, A. Bochem, K. G. Hovingh, E. B. Thorp, E. L. Gautier, D. Kratky, P. Dasilva-Jardine, L. Yvan-Charvet, *Circ. Res.* **2018**, *122*, 1369.
- [34] P. A. Betancur, B. J. Abraham, Y. Y. Yiu, S. B. Willingham, F. Khameneh, M. Zarnegar, A. H. Kuo, K. McKenna, Y. Kojima, N. J. Leeper, P. Ho, P. Gip, T. Swigut, R. I. Sherwood, M. F. Clarke, G. Somlo, R. A. Young, I. L. Weissman, *Nat. Commun.* **2017**, *8*, 14802.
- [35] Z. Zheng, N. Chinnasamy, R. A. Morgan, *J. Transl. Med.* **2012**, *10*, 29.
- [36] X. Liu, R. Ranganathan, S. Jiang, C. Fang, J. Sun, S. Kim, K. Newick, A. Lo, C. H. June, Y. Zhao, E. K. Moon, *Cancer Res.* **2016**, *76*, 1578.
- [37] Z. Lv, Z. Bian, L. Shi, S. Niu, B. Ha, A. Tremblay, L. Li, X. Zhang, J. Paluszynski, M. Liu, K. Zen, Y. Liu, *J. Immunol.* **2015**, *195*, 661.
- [38] K. Taruc, C. Yin, D. G. Wootton, B. Heit, *J. Vis. Exp.* **2018**, *138*, 58149.
- [39] C. Guo, W. Kong, K. Kamimoto, G. C. Rivera-Gonzalez, X. Yang, Y. Kirita, S. A. Morris, *Genome Biol.* **2019**, *20*, 90.
- [40] a) E. Thorp, T. Vaisar, M. Subramanian, L. Mautner, C. Blobel, I. Tabas, *J. Biol. Chem.* **2011**, *286*, 33335; b) B. Cai, E. B. Thorp, A. C. Doran, M. Subramanian, B. E. Sansbury, C. S. Lin, M. Spite, G. Fredman, I. Tabas, *Proc. Natl. Acad. Sci. U. S. A.* **2016**, *113*, 6526.
- [41] S. G. Thacker, A. Zazour, Y. Chen, M. S. Alciçek, L. A. Freeman, D. O. Sviridov, S. J. Demosky Jr., A. T. Remaley, *Immunology* **2016**, *149*, 306.
- [42] a) P. Ochtrup, C. P. R. Hackenberger, *Curr. Opin. Chem. Biol.* **2020**, *58*, 28; b) J. F. Ponte, X. Sun, N. C. Yoder, N. Fishkin, R. Laleau, J. Coccia, L. Lanieri, M. Bogalhas, L. Wang, S. Wilhelm, W. Widdison, J. Pinkas, T. A. Keating, R. Chari, H. K. Erickson, J. M. Lambert, *Bioconjugate Chem.* **2016**, *27*, 1588; c) K. Renault, J. W. Fredy, P.-Y. Renard, C. Sabot, *Bioconjugate Chem.* **2018**, *29*, 2497; d) J. You, J. Zhang, J. Wang, M. Jin, *Bioconjugate Chem.* **2021**, *32*, 1525.
- [43] a) E. A. Ho, M. Osooly, D. Strutt, D. Masin, Y. Yang, H. Yan, M. Bally, *J. Pharm. Sci.* **2013**, *102*, 227; b) S. H. Lee, Y. Sato, M. Hyodo, H. Harashima, *Biol. Pharm. Bull.* **2017**, *40*, 1002; c) I. Menon, M. Zaroudi, Y. Zhang, E. Aisenbrey, L. Hui, *Mater. Today Adv.* **2022**, *16*, 100299.
- [44] V. Golubovskaya, R. Berahovich, H. Zhou, S. Xu, H. Harto, L. Li, C. C. Chao, M. M. Mao, L. Wu, *Cancers* **2017**, *9*, 139.
- [45] M. Patel, Y. Li, J. Anderson, S. Castro-Pedrido, R. Skinner, S. Lei, Z. Finkel, B. Rodriguez, F. Esteban, K.-B. Lee, Y. L. Lyu, L. Cai, *Mol. Ther.* **2021**, *29*, 2469.
- [46] S. E. Çelik, M. Özyürek, K. Güçlü, R. Apak, *Journal of Inclusion Phenomena and Macrocyclic Chemistry* **2015**, *83*, 309.